Materials Advances

ROYAL SOCIETY OF CHEMISTRY

PAPER

View Article Online
View Journal | View Issue

Cite this: *Mater. Adv.*, 2026, 7, 1737

Comprehensive structure–property–function correlation in three hybrid Bi(III) and Sb(III) metal halide compounds based on 4-ethylaminomethylpyridine: comparative insights into optical, dielectric, and antibiological activities

Amin Alibi,[a] Sameh Sellami,[b] Fatma El Abed,[b] Nour Elleuch,[a] Jerome Lhoste,[c] Guillaume Duval[c] and Mohamed Boujelbene *[a]

Three new hybrid halometallates, $(C_8H_{14}N_2)_2[Bi_2Br_{10}]\cdot 2H_2O$ (**M4**), $(C_8H_{14}N_2)_3[BiCl_6]_2$ (**M43**), and $(C_8H_{14}N_2)[SbCl_5]$ (**M41**), have been comparatively investigated to establish comprehensive structure–property–function correlations. Single-crystal X-ray diffraction analysis revealed distinct zero-dimensional motifs based on Bi_2Br_{10} dimers, $BiCl_6$ octahedra, and $SbCl_5$ square pyramids, with packing efficiencies ranging from 92.9 to 94.1%. These structural differences directly modulate their optical and dielectric properties: **M4** exhibits broadband photoluminescence at 470 nm and an intermediate band gap of 2.90 eV; **M43**, the most distorted and least dense phase, displays a wide band gap of 3.16 eV with suppressed PL; and **M41**, with a nearly ideal square-pyramidal $SbCl_5$ geometry, shows the narrowest gap (2.77 eV) and a clean green–yellow emission at 571 nm, alongside dynamic dielectric relaxation processes. Antibacterial assays revealed exceptional activity for the organic cation and **M41**, surpassing that of gentamicin against both Gram-positive and Gram-negative strains, whereas **M4** and **M43** were significantly less active due to stronger ion pairing and reduced cation release. This integrated analysis highlights the pivotal roles of halide identity, metal coordination geometry, and lattice topology in dictating multifunctionality. The findings establish anion–cation engineering in halometallates as a versatile platform for designing materials that simultaneously combine optical, dielectric, and antibacterial properties.

Received 31st October 2025,
Accepted 17th December 2025

DOI: 10.1039/d5ma01261a

rsc.li/materials-advances

1. Introduction

Hybrid organic–inorganic halometallates have emerged as a versatile class of multifunctional materials that combine the structural diversity of molecular crystals with the electronic robustness of inorganic frameworks.[1–3] This dual nature enables fine control over their optical, electronic, dielectric, and even biological properties, making these systems attractive for applications spanning optoelectronics, sensing, energy conversion, and biomedical platforms.[4–6] The modular construction of hybrid halometallates, achieved through independent variation of the organic cation, metal center, and halide ligands, provides a powerful synthetic handle to tailor band structures, exciton confinement, dielectric responses, and structural stabilities.[7,8]

A central feature governing the properties of hybrid halometallates is the interplay between organic and inorganic sublattices. In low-dimensional systems, particularly those constructed from isolated or pseudo-isolated metal–halide units, this interplay becomes especially transparent, allowing subtle structure–property relationships to be examined with minimal topological complexity.[9] Such zero-dimensional (0D) architectures suppress long-range electronic delocalization and amplify the influence of local coordination geometry, metal–halide bonding, and supramolecular interactions on optical absorption, emission behavior, and dielectric relaxation processes.

Among the various metal centers explored, bismuth(III) and antimony(III) are of particular interest as environmentally benign alternatives to lead-based systems. Both cations exhibit stereoactive ns^2 lone pairs ($6s^2$ for Bi^{3+} and $5s^2$ for Sb^{3+}), which induce local structural distortions and strongly influence

[a] *Laboratory of Physico-Chemistry of Solid State, LR11ES51, Sfax Faculty of Sciences, University of Sfax, Sfax 3000, Tunisia*
[b] *Biopesticides Laboratory, Centre of Biotechnology of Sfax, Sfax University, P.O. Box 1177, 3018, Sfax, Tunisia*
[c] *MMM-UMR 6283 CNRS, Lunam, Faculty of Sciences and Techniques, University of Maine, Avenue Olivier Messiaen, 72085, Le Mans Cedex 9, France*

their electronic structures, optical transitions, and lattice polarizability.[10,11] In parallel, the nature of the halide ligand (Cl^- *vs.* Br^- *vs.* I^-) plays a decisive role in tuning metal–halide covalency, band gap energies, and excitonic effects.[12] As a result, targeted metal and halide substitution has become a widely adopted strategy for engineering hybrid halometallates with tailored functionalities.[13–15]

Despite these advances, most reported studies on Bi(III)- and Sb(III)-based hybrid halometallates remain largely confined to isolated systems, in the sense that they typically focus on a single compound and investigate one dominant property, most often optical absorption or photoluminescence, without systematic comparison across closely related compositions. For example, several 0D Bi–Cl hybrid halometallates have been reported to exhibit indirect band gaps in the range of 3.3–3.4 eV, with investigations restricted primarily to solid-state optical characterization.[16,17] In contrast, Sb–Cl hybrids with similar low-dimensional architectures have been shown to display direct band gaps and, in some cases, additional biological activity, yet these systems are likewise examined independently, without direct structural or compositional benchmarking against Bi-based analogues.[18] Such fragmented approaches limit the ability to establish robust correlations between metal identity, halide substitution, structural motifs (monomeric *versus* dimeric units), and multifunctional properties.

Consequently, there remains a clear need for comprehensive, comparative investigations that integrate crystallographic, spectroscopic, optical, dielectric, and theoretical analyses within unified families of hybrid halometallates. Only through such systematic studies can reliable structure–property–function relationships be established, providing predictive guidelines for rational materials design.

In response to this challenge, we report herein the synthesis and comparative investigation of three new hybrid halometallates based on a common organic cation, 4-ethylaminomethylpyridine: $(C_8H_{14}N_2)_2[Bi_2Br_{10}]\cdot 2H_2O$,[19] $(C_8H_{14}N_2)_3[BiCl_6]_2$,[20] and $(C_8H_{14}N_2)[SbCl_5]$.[21,22] The use of an identical organic component across all compounds ensures a consistent supramolecular environment, enabling a focused assessment of how metal center substitution (Bi^{3+} *vs.* Sb^{3+}) and halide identity (Br^- *vs.* Cl^-) govern structural dimensionality, electronic structure, and functional response.

Single-crystal X-ray diffraction was employed to elucidate coordination geometries, dimensionalities, and hydrogen-bonding networks stabilizing the crystalline architectures,[1] complemented by FTIR and Raman spectroscopies to probe bonding environments and lattice dynamics.[2,3] Optical absorption studies in both solid and solution states provided insight into electronic transitions and band gap characteristics,[4,5] while density functional theory (DFT) and time-dependent DFT calculations were used to analyze frontier orbital distributions and electronic features.[6,7] Intermolecular interactions were further examined through Hirshfeld surface analysis and reduced density gradient (RDG) mapping, highlighting the role of non-covalent forces in supramolecular stabilization.[8,9] Dielectric relaxation and impedance behavior were investigated by electrochemical impedance spectroscopy (EIS), particularly for Sb-based systems where enhanced ionic mobility is anticipated.[10]

Beyond structural and physicochemical characterization, preliminary evaluations of antibiological activity were undertaken to explore the broader multifunctional potential of these hybrid halometallates, extending their relevance beyond conventional optoelectronic applications.[11] By correlating metal identity, halide composition, structural motifs, and supramolecular organization with optical, dielectric, and biological responses, this work provides a unified framework for understanding and designing next-generation Bi(III)- and Sb(III)-based hybrid halometallates with tailored multifunctional properties.[12–15]

2. Experimental

2.1. Materials and reagents

All chemical reagents used in this study were of analytical grade and employed without additional purification. Antimony(III) chloride ($SbCl_3$, 99.95% purity), bismuth(III) chloride ($BiCl_3$, 99.9% purity), bismuth(III) bromide ($BiBr_3$, 99.9% purity), and the organic ligand 4-(ethylaminomethyl) pyridine ($C_8H_{14}N_2$, $\geq$97% purity) were all sourced from Sigma-Aldrich. Concentrated hydrobromic acid (HBr, 48%) and concentrated hydrochloric acid (HCl, 37–38% aqueous solution) were also obtained from Sigma-Aldrich.

All solution preparations and crystallizations were performed using freshly distilled water to ensure reproducible crystal growth and to minimize contamination from extraneous ionic species. No further purification, recrystallization, or drying of the starting materials was undertaken. All synthetic procedures and characterization experiments were conducted under standard laboratory conditions (25–30 °C).

2.2. Synthesis procedures

All three bismuth-based and antimony-based halide hybrid compounds, $(C_8H_{14}N_2)_2[Bi_2Br_{10}]\cdot 2H_2O$, $(C_8H_{14}N_2)_3[BiCl_6]_2$, and $(C_8H_{14}N_2)[SbCl_5]$, were synthesized using a slow evaporation technique under ambient conditions, as described in detail in our earlier work.[19–21] Briefly, each metal halide precursor ($BiBr_3$, $BiCl_3$, or $SbCl_3$) was reacted with the organic ligand $C_8H_{14}N_2$ in aqueous solution, with acid (HBr or HCl) added to stabilize the respective halometallate species. For compounds **M4** and **M41**, the organic ligand and inorganic precursor were used in a 1 : 1 molar ratio (1.0 mmol each), whereas **M43** was synthesized using a 3 : 2 organic–inorganic molar ratio (1.5 mmol organic ligand and 1.0 mmol inorganic precursor). All syntheses were conducted on a molar basis and can be proportionally scaled while preserving the same stoichiometric ratios. The resulting homogeneous mixtures were filtered and left to evaporate slowly at room temperature, yielding well-formed single crystals within 4–10 days, depending on the system. Specific stoichiometric adjustments were employed to guide the crystallization toward the desired $[Bi_2Br_{10}]^{4-}$ dimeric units, isolated $[BiCl_6]^{3-}$ octahedra, or distorted $[SbCl_5]^{2-}$

geometries. Crystals were harvested, washed with a small amount of alcohol, and dried carefully to preserve phase integrity.

The purity of these two hybrid materials was confirmed through both powder XRD and EDS with elemental mapping, indicating that the compounds are highly pure, as can be seen in Fig. S1 and S2.

2.3. Characterization techniques

An array of complementary characterization techniques were employed to thoroughly investigate the synthesized compounds' structural, vibrational, optical, and electrical properties.

Single-crystal data were collected using an XtaLAB Synergy, Dualflex, HyPix diffractometer with Mo-Kα radiation (λ = 0.71073 Å). Unit cell determination, data reduction, and absorption corrections were performed using the CrysAlisPro software suite.[23] Structures were solved by intrinsic phasing using SHELXT 2018/2 and refined against F^2 by full-matrix least-squares methods with SHELXL 2018/3.[24,25] Comprehensive crystallographic refinement details and comparison of these three compounds, including key structural parameters, are systematically compiled in Table 1.

FTIR spectra were recorded using a PerkinElmer FT-IR Paragon 1000 PC spectrometer operating in the range 4000–500 cm^{-1}. Raman spectra were obtained using a Horiba/Jobin-6 Yvon T6400 spectrometer. The spectral range covered 50–4000 cm^{-1} with a spectral resolution equal to 2 cm^{-1}. Optical absorption measurements were carried out both in aqueous solution and in the solid state using the diffuse reflectance mode. The spectrophotometer was a PerkinElmer Lambda 35 with an integrating sphere. Solid-state data were processed *via* the Kubelka–Munk transformation to determine optical band gaps. PL measurements were conducted using a PerkinElmer LS 55 fluorescence spectrometer, employing a xenon lamp as the excitation source. Excitation and emission spectra were recorded at room temperature. EIS measurements were performed only for $(C_8H_{14}N_2)[SbCl_5]$ using a Solartron SI 1260 gain-phase analyzer over the frequency range 40 Hz–10^7 Hz. Measurements were conducted under a temperature-controlled environment between 40 and 140 °C, allowing assessment of dielectric and relaxation properties.

2.4. Computational details

All theoretical calculations were carried out using the Gaussian 09W suite.[26] Geometry optimizations were performed using the hybrid B3LYP functional in conjunction with the LanL2DZ basis set,[27,28] well-suited for heavy atoms like Bi and Sb. No symmetry constraints were imposed during optimization. Frequency calculations confirmed the nature of the stationary points as true minima (no imaginary frequencies).

TD-DFT calculations were performed to simulate UV-Vis absorption spectra and analyze optical transitions. Cluster models, extracted from experimental crystal structures, were constructed to preserve critical intra- and intermolecular interactions. Frontier molecular orbitals (HOMO and LUMO), density of states (DOS), and partial DOS (PDOS) were computed.

The electronic distributions were analyzed using the Multiwfn 3.8 package,[29] generating molecular electrostatic potential (ESP) maps, electron localization function (ELF), and localized orbital

Table 1 Summary of crystal data and structure refinement details for **M4**, **M41**, and **M43**

Crystallographic data			
Empirical formula	$(C_8H_{14}N_2)_2[Bi_2Br_{10}]\cdot 2H_2O$[19]	$(C_8H_{14}N_2)\cdot[SbCl_5]$[20]	$(C_8H_{14}N_2)_3[BiCl_6]_2$[21]
Color/Shape	Yellow plate	Clear light block	Clear light block
Mass molar (g mol^{-1})	1529.51	437.21	1257.99
Diffractometer	XtaLAB synergy, dualflex, HyPix diffractometer	XtaLAB synergy, dualflex, HyPix diffractometer	XtaLAB synergy, dualflex, HyPix diffractometer
Radiation type	Mo Kα (0.71073 Å)	Mo Kα (0.71073 Å)	Mo Kα (0.71073 Å)
Temperature (K)	293	100	293
Calculated density (Mg m^{-3})	2.95	1.972	1.846
Crystal system	Monoclinic	Monoclinic	Monoclinic
Space group	$P2_1/c$	$P2_1/n$	$P2_1/n$
Z/Z'	2/0.5	4	4
Unit cell parameters			
a (Å)	10.6409 (2)	10.8365 (3)	15.1677 (3)
b (Å)	12.0862 (2)	11.8067 (3)	11.9461 (2)
c (Å)	14.1356 (4)	12.0281 (3)	25.6539 (5)
β (°)	108.685 (3)	106.920 (3)	103.092 (2)
Absorption coefficient (mm^{-1})	21.83	2.76	8.49
		0.15 × 0.15 × 0.1	0.17 × 0.13 × 0.08
Number of reflections measured variation of h, k, l	$h = -12 \rightarrow 12$, $k = -13 \rightarrow 14$, $l = -16 \rightarrow 16$	$h = -12 \rightarrow 13$, $k = -11 \rightarrow 16$, $l = -15 \rightarrow 12$	$h = -18 \rightarrow 18$, $k = -14 \rightarrow 14$, $l = -30 \rightarrow 30$
Scanning range of θ(°)	$2.6 < \theta < 30.2$	$2.5 < \theta < 30.4$	$2.5 \rightarrow 25$
F(000)	1376	848	2392
Independent parameters	159	146	400
$\Delta\rho_{max}/\Delta\rho_{min}$ (e $Å^{-3}$)	1.89/−1.05	0.48/−0.49	0.56/−0.55
(Δ/σ)max	<0.001	<0.001	<0.003
$R[F^2 > 2\sigma(F^2)] = R_1$	0.023	0.0218	0.0218
$wR(F^2) = wR_2$	0.055	0.0444	0.0444
S = GooF	1.07	1.05	1.05
CCDC	2384365	2382366	2432091

locator (LOL) surfaces. Non-covalent interactions were analyzed through the reduced density gradient (RDG) method to identify weak interactions like hydrogen bonds, halogen bonds, and van der Waals forces.

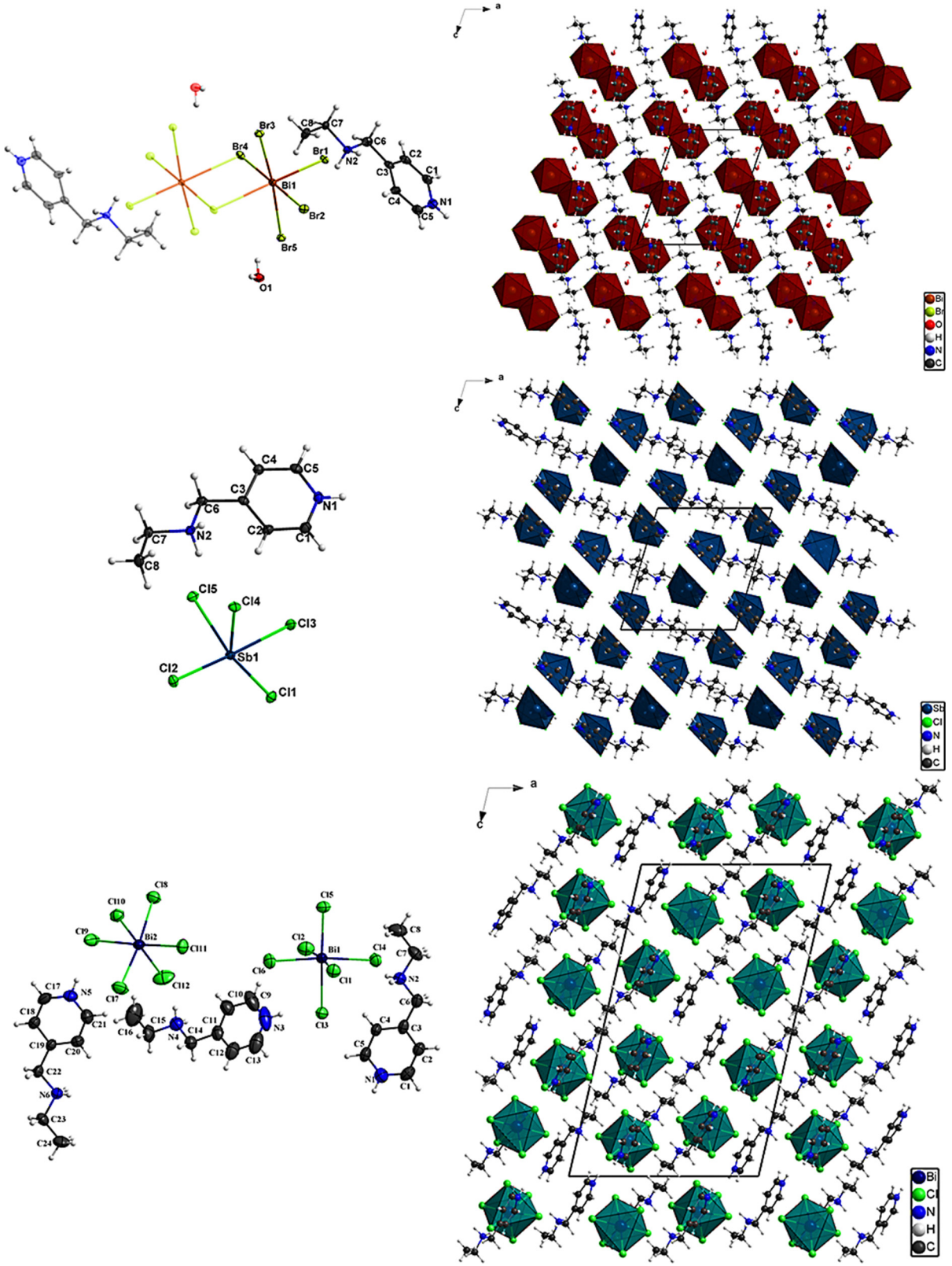

Fig. 1 Comparison of the principal hydrogen bonds in the three compounds: (a) **M4**, (b) **M41**, and (c) **M43**.

All graphical visualizations (orbitals, surfaces, and RDG isosurfaces) were rendered with GaussView 6.0.16.[30] The theoretical results were systematically compared with the experimental observations to validate the findings and provide deeper insights into structure–property relationships.

2.5. Antibiological activity tests

The antibacterial activity of the synthesized compounds was evaluated using the standard agar well diffusion method against five pathogenic bacterial strains: two Gram-positive (*Staphylococcus aureus* and *Bacillus cereus*) and three Gram-negative (*Pseudomonas aeruginosa*, *Enterococcus faecalis*, and *Salmonella typhimurium*). Fresh bacterial suspensions were prepared at a concentration of 10^6 CFU mL^{-1}, and 100 μL of each suspension was evenly spread onto nutrient agar plates. Wells of approximately 10 mm in diameter were aseptically bored into the agar using a sterile cork borer. A volume of 100 μL of the test solutions, prepared at a concentration of 1 mg mL^{-1} for all hybrid compounds and their free organic cation, was introduced into the wells. The plates were incubated at 37 °C for 24 hours under sterile conditions. Following incubation, the antibacterial activity was quantified by measuring the diameter of the inhibition zones (in mm) formed around each well. The organic precursor 4-(ethylaminomethyl)pyridine was used as a negative control, while the aminoglycoside antibiotic gentamicin (15 μg per well) served as the positive control. All experiments were performed in triplicate to ensure reproducibility, and the results are reported as average inhibition zone diameters.

3. Results and discussion

3.1. Crystallographic features and molecular arrangement

Single-crystal X-ray diffraction analyses provided comprehensive insights into the crystallographic features, coordination geometries, and supramolecular architectures of the three hybrid halometallates under study. Although all compounds share the general theme of organic–inorganic hybrid frameworks based on metal–halide complexes and protonated organic cations, and the same dimensionality, significant differences in structural distortion and intermolecular interactions were observed, depending on the halogen and the central metal cation (Fig. 1).

4-Ethylaminomethylpyridine was selected as the organic component due to its bifunctional nature and strong hydrogen-bonding ability. Upon protonation under the synthesis conditions, the molecule forms a stable organic cation containing both a pyridinium nitrogen and a protonated amine group, enabling multiple N–H···X (X = Cl, Br) hydrogen-bond interactions with the inorganic halometallate units. Its moderate steric bulk and conformational flexibility allow effective charge compensation and stabilization of zero-dimensional inorganic motifs while preventing framework polymerization. In addition, the organic cation is chemically stable and optically inactive in the visible region, ensuring that the observed optical properties originate predominantly from the inorganic sublattice.

The compound $(C_8H_{14}N_2)_2[Bi_2Br_{10}]\cdot 2H_2O$ crystallizes in the monoclinic crystal system, adopting the $P2_1/c$ space group. Its

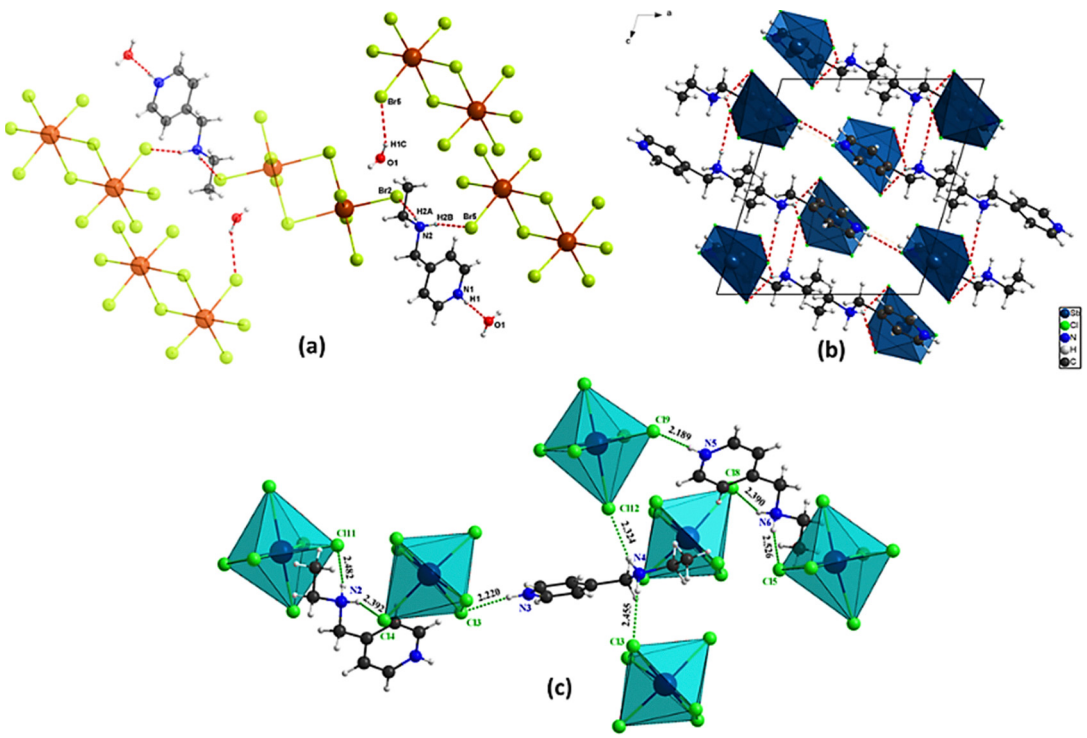

Fig. 2 Representation of the formula units, their dimensionality, and crystalline architectures, as well as the molecular arrangements of the compounds (a) **M4**, (b) **M41**, and (c) **M43** along the *b* axis.

structure is based on discrete $[Bi_2Br_{10}]^{4-}$ dimers, in which two Bi^{3+} centers are each coordinated octahedrally by six bromide ions, with two bridging bromides linking the bismuth atoms. The Bi–Br bond lengths range between 2.7271(5) and 3.0612(5) Å, indicating very slight distortions from ideal octahedral symmetry, as the $6s^2$ lone pair on Bi^{3+} is essentially inert in this case. The dimeric units are spatially separated by protonated 4-(ethylaminomethyl) pyridine cations and water molecules, which interact through a rich hydrogen-bonding network (N–H···Br and O–H···Br) that extends three-dimensionally, contributing to structural cohesion (Fig. 2(a)). Notably, the incorporation of lattice water molecules enhances the hydrogen bonding density, promoting additional stabilization of the crystal lattice.

In contrast, $(C_8H_{14}N_2)_3[BiCl_6]_2$ crystallizes in the triclinic $P\bar{1}$ space group, with a markedly different structural motif. The inorganic moiety consists of isolated, discrete $[BiCl_6]^{3-}$ octahedral anions, in which each Bi^{3+} center is surrounded by six chloride ions with bond distances spanning 2.5965(16) to 2.8387(17) Å. Compared to the bromide-based dimer, the chloride-based units exhibit somewhat greater distortion, attributable to the stereoactive $6s^2$ lone pair on Bi^{3+}. The $[BiCl_6]^{3-}$ octahedra are embedded in a hydrogen-bonded matrix formed by three protonated 4-(ethylaminomethyl) pyridine cations per two octahedra, generating a compact but less dense arrangement relative to the bromide system. The absence of lattice water molecules results in a solvent-free network primarily involving N–H···Cl interactions (Fig. 2(c)), though the crystal void analysis indicates a higher void fraction of 10.2%.

The third compound, $(C_8H_{14}N_2)[SbCl_5]$, adopts a monoclinic $P2_1/n$ space group and features zero-dimensional $[SbCl_5]^{2-}$ units, where the Sb^{3+} ions are coordinated by five chlorine atoms in a near-perfect square-pyramidal geometry. The primary Sb–Cl bond lengths range from 2.4234(5) to 2.9774(5) Å, while weaker secondary interactions ($\sim$3.212(2) Å) link neighboring anions, creating a pseudo-chain-like arrangement. This partial connectivity contrasts with the isolated nature of $[BiCl_6]^{3-}$ units and the dimeric $[Bi_2Br_{10}]^{4-}$ structures. The organic cations are intercalated between these units, stabilizing the structure *via* hydrogen bonds (N–H···Cl) and van der Waals interactions (Fig. 2(b)). The distortion around Sb^{3+} is more pronounced than that around Bi^{3+}, in agreement with the stereoactive $5s^2$ lone pair and the greater flexibility of the pentacoordinate environment, but still a slight distortion compared to $(C_8H_{14}N_2)_3[BiCl_6]_2$.

Analysis of the packing arrangements reveals important structural differences among the three 0D compounds. In $(C_8H_{14}N_2)_2[Bi_2Br_{10}]\cdot 2H_2O$, the crystal structure exhibits a low void volume of 5.9%, indicative of a highly efficient packing despite the inclusion of water molecules, which are accommodated within small residual cavities. This compact arrangement suggests strong intermolecular interactions and minimal unoccupied space. The structure of $(C_8H_{14}N_2)[SbCl_5]$ displays a slightly higher void space of 7.1%, corresponding to moderately less dense packing, influenced by the spatial distribution of the organic cations around the pseudo-polymeric $[SbCl_5]^{2-}$ units. For $(C_8H_{14}N_2)_3[BiCl_6]_2$, the packing is less efficient, with a void volume of 10.2%, reflecting looser organization despite the solvent-free hydrogen-bonded framework.

The hydrogen-bonding network plays an important structural role by stabilizing the crystal packing and reducing local dynamic disorder. This lattice rigidification indirectly influences optical behavior by modulating metal–halide distortions and vibrational relaxation pathways, without contributing electronic states near the band edges.

From a symmetry perspective, the crystallographic progression from monoclinic $P2_1/c$ in the bromide dimer compound to triclinic $P\bar{1}$ in the chloride-based isolated octahedral structure, and then to monoclinic $P2_1/n$ in the chloride compound containing discrete $[SbCl_5]^{2-}$ units, underscores the nuanced interplay between the metal center (Bi *vs.* Sb), the halide identity (Br^- *vs.* Cl^-), and the configuration of the anionic substructure. While all three compounds are based on 0D structural units, the distinct nature of the inorganic moieties, ranging from edge-sharing $[Bi_2Br_{10}]^{4-}$ dimers to isolated $[BiCl_6]^{3-}$ octahedra and pseudo-polymeric $[SbCl_5]^{2-}$ anions, results in variations in packing density, hydrogen-bonding networks, and supramolecular organization. These crystallographic transformations reflect how small changes in composition and coordination geometry influence the global symmetry and internal ordering of the crystal lattice. This structural evolution has direct implications for the physical properties, as elaborated in subsequent sections. Overall, the crystallographic analysis reveals that the combined effects of halide type, metal identity, and anionic architecture collectively dictate the molecular geometry, packing efficiency, and overall stability of these hybrid organic–inorganic systems. All these structural details are conveniently summarized in Table S1 for clarity and direct comparison.

Beyond the descriptive crystallographic differences, the observed variations in coordination geometry, packing density, and hydrogen-bond topology provide a direct structural basis for the contrasting physical properties discussed in the following sections. The highly compact and weakly distorted $[Bi_2Br_{10}]^{4-}$ dimeric units in **M4**, combined with the dense hydrogen-bonding network reinforced by lattice water molecules, result in a rigid inorganic sublattice with limited structural flexibility. Such rigidity favors strong lattice cohesion but suppresses large-amplitude metal–halide distortions, a factor that is consistent with moderate electronic localization and reduced ionic mobility. In contrast, the isolated $[BiCl_6]^{3-}$ octahedra in **M43**, embedded within a more weakly packed and void-rich lattice, experience enhanced static distortion arising from the stereoactive $6s^2$ lone pair of Bi^{3+}. This distortion disrupts electronic delocalization and contributes to the wider band gap and suppressed photoluminescence observed for this compound. The Sb-based compound **M41** occupies an intermediate but structurally distinctive position, where the square-pyramidal $[SbCl_5]^{2-}$ units introduce pronounced asymmetry while maintaining a relatively ordered packing arrangement. This balance between distortion and structural coherence is expected to promote localized electronic states while still allowing sufficient lattice adaptability, a

combination that later manifests in its distinctive optical emission and dielectric response.

From a comparative perspective, the progression from dimeric $[Bi_2Br_{10}]^{4-}$ units to isolated $[BiCl_6]^{3-}$ octahedra and finally to pseudo-connected $[SbCl_5]^{2-}$ units highlights how subtle changes in metal identity and halide chemistry modulate both local coordination environments and long-range supramolecular organization. The larger, more polarizable Br^- ligands in **M4** favor extended dimer formation and dense packing, whereas the smaller Cl^- ligands promote isolated coordination motifs with increased distortion and void space. Substitution of Bi^{3+} by Sb^{3+} further amplifies these effects due to the stronger stereoactivity of the $5s^2$ lone pair, which stabilizes lower coordination numbers and anisotropic geometries. These crystallographic distinctions are not merely structural curiosities; they establish the framework for understanding the divergent optical band gaps, dielectric relaxation behavior, and ionic mobility trends observed experimentally. Thus, the crystallographic analysis serves as a foundational link between composition, structure, and multifunctional performance, demonstrating that even within a shared zero-dimensional motif, targeted chemical modifications can yield markedly different physical outcomes.

3.2. Non-covalent interactions and Hirshfeld surface analysis

To deepen the understanding of the intermolecular interactions and packing features in the three compounds, detailed Hirshfeld surface (HS) analyses were conducted. The three-dimensional HS mapped over the normalized contact distance (d_{norm}), two-dimensional fingerprint plots (FPs), and quantitative interaction contributions were systematically compared to unveil the nature and strength of non-covalent forces stabilizing each crystal structure (Fig. 3).

For $(C_8H_{14}N_2)_2[Bi_2Br_{10}]\cdot 2H_2O$, the Hirshfeld surface revealed prominent and localized red depressions corresponding to intense Br···H and H···Br contacts, confirming strong hydrogen bonding between the organic cations and the bromide-rich inorganic sublattice. Quantitative fingerprint analysis showed that H···Br/Br···H contacts contributed 57.6% to the total surface area, establishing them as the dominant interaction. This was followed by H···H contacts at 22.5%, representative of close-range van der Waals contacts between adjacent alkyl and amine hydrogen atoms. C···H/H···C contacts accounted for 10.9%, while Br···Br interactions contributed 3.4%, pointing to possible dispersion-driven halogen contacts that reinforce supramolecular packing. The fingerprint plot exhibited sharp, well-defined spikes at short di and de values, reinforcing the presence of directional hydrogen bonds and dense packing topology.

In comparison, $(C_8H_{14}N_2)_3[BiCl_6]_2$ displayed a smoother and less topographically complex Hirshfeld surface, dominated by H···Cl/Cl···H interactions, which accounted for 64.4% of the surface area. This interaction is indicative of N–H···Cl and C–H···Cl hydrogen bonding between the organic cations and the discrete $[BiCl_6]^{3-}$ anions. The H···H contacts made up 24.8%, reflecting relatively efficient but non-directional packing among organic species. C···H/H···C interactions contributed 7.0%, while Cl···Cl interactions contributed a minor 2.0%, consistent with weak but detectable halogen–halogen contacts. The 2D fingerprint plots revealed narrow spikes near di ≈ de ≈ 1.8 Å, typical of moderately strong hydrogen bonds, and highlighted a compact yet non-polar interaction landscape.

For $(C_8H_{14}N_2)[SbCl_5]$, the Hirshfeld surface displayed broad red regions, revealing an interaction pattern that bridges the features observed in the previous two compounds. The dominant H···Cl/Cl···H interactions contributed 59.1%, underscoring their role in N–H···Cl hydrogen bonding with the chloridoantimonate polyhedra. H···H interactions accounted for 18.7%, lower than in the bismuth analogues, but suggestive of tighter or more efficient organic chain packing. Notably, C···H/H···C contacts contributed 9.4%, while Cl···Cl interactions contributed 2.6%, implying a modest halogen–halogen role in stabilizing the structure. The broader, less symmetrical distribution of the fingerprint spikes reflects a more spatially flexible or less ordered hydrogen-bonding network.

A comparative analysis of the three compounds indicates that the nature of the halogen (Cl^- *vs.* Br^-) significantly influences both the interaction profile and the packing density. In $(C_8H_{14}N_2)_2[Bi_2Br_{10}]\cdot 2H_2O$, the larger and more polarizable bromide ions promote stronger yet slightly longer hydrogen bonds, giving rise to a more corrugated Hirshfeld surface characterized by intense red spots. The fingerprint plot confirms that H···Br/Br···H contacts contribute 57.6%, with additional contributions from H···H (22.5%), C···H (10.9%), and Br···Br (3.4%), indicating a complex balance of directional hydrogen bonding and weaker dispersive contacts. In contrast, the chloride-based compounds, $(C_8H_{14}N_2)_3[BiCl_6]_2$ and $(C_8H_{14}N_2)[SbCl_5]$, feature smaller, more electronegative halide ions, favoring shorter, more directional hydrogen bonds that drive denser and more isotropic packing. The $[BiCl_6]^{3-}$ compound exhibits a smoother Hirshfeld surface dominated by H···Cl/Cl···H contacts (64.4%), followed by H···H (24.8%), C···H (7.0%), and Cl···Cl (2.0%) interactions. Substitution of Bi^{3+} by Sb^{3+} in the $[SbCl_5]^{2-}$ analogue leads to subtle changes in the chloride coordination geometry and the surrounding interaction field, reflected by broader and less symmetric fingerprint distributions. In this case, H···Cl/Cl···H contacts comprise 59.1%, with H···H (18.7%), C···H (9.4%), and Cl···Cl (2.6%) contributions. These distinctions are further echoed in the crystal symmetries: monoclinic $P2_1/c$ for the bromide dimer, triclinic $P\bar{1}$ for the Bi–Cl octahedral system, and monoclinic $P2_1/n$ for the Sb–Cl compound. Thus, Hirshfeld surface analysis provides compelling evidence that, although hydrogen bonding is the predominant interaction across all three hybrid halometallates, the detailed balance between different contact types and the resulting packing motifs are sensitively tuned by the halogen type (Br^- *vs.* Cl^-) and the nature of the central metal cation (Bi^{3+} *vs.* Sb^{3+}).

3.3. Vibrational spectral analysis (FTIR and Raman)

Vibrational spectroscopy, through Fourier-transform infrared (FTIR) (Fig. S3) and Raman analyses (Fig. S4), was employed to probe the fundamental bonding environments and confirm the structural integrity of the three synthesized compounds. Both

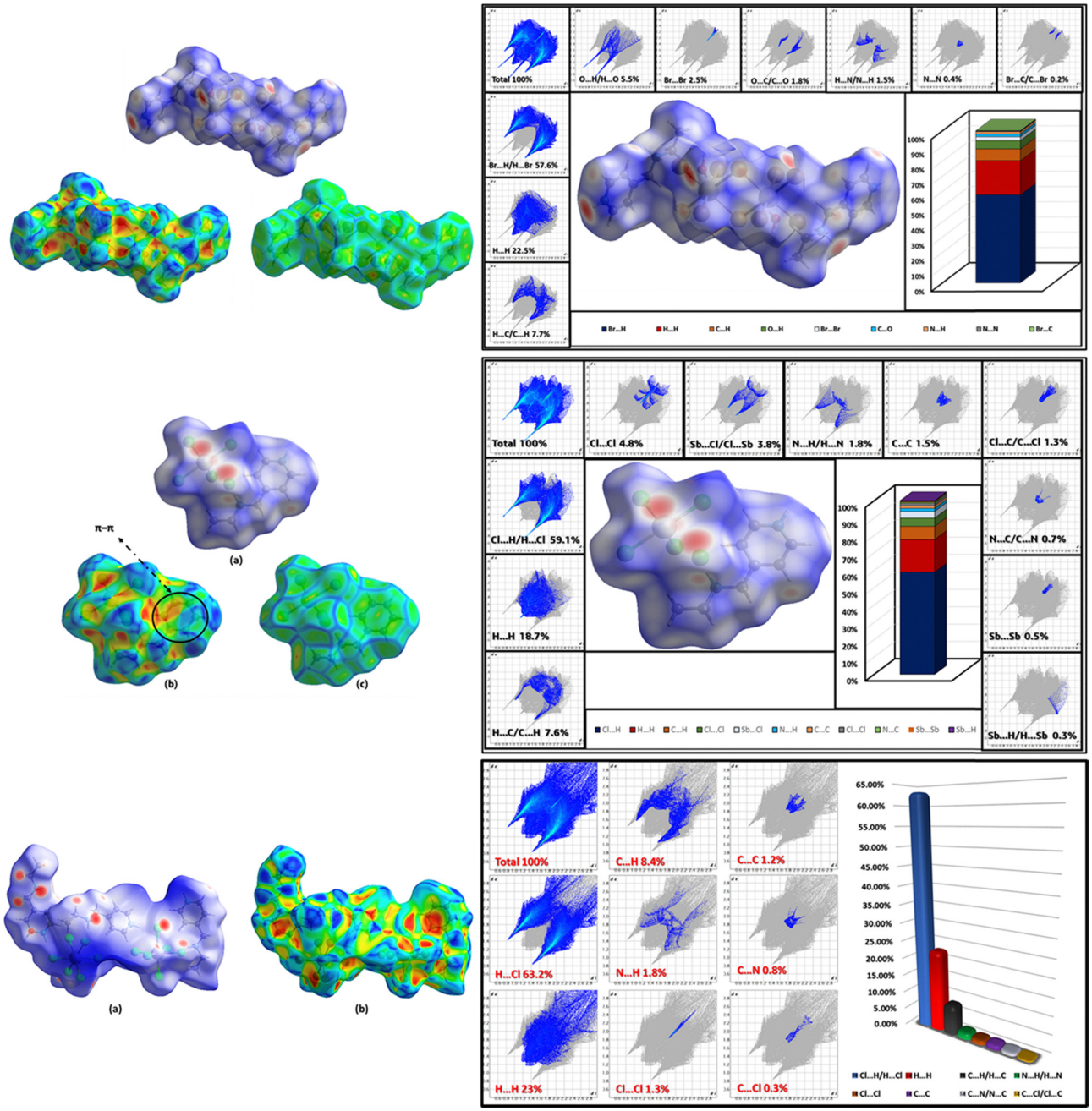

Fig. 3 Hirshfeld surface analyses and the fingerprint of compounds: (a) **M4**, (b) **M41**, and (c) **M43**.

experimental and theoretical (DFT) investigations were utilized to assign vibrational modes and highlight structure-dependent variations among the materials.

In the FTIR spectra, all three compounds exhibited characteristic bands associated with the organic moiety ($C_8H_{14}N_2$), primarily stemming from stretching and bending vibrations of C–H, C–C, and C–N bonds. Broad absorptions observed in the region between 3200–3400 cm^{-1} were assigned to N–H stretching vibrations from protonated nitrogen atoms involved in hydrogen bonding with halide ions. Notably, the stretching bands appeared slightly redshifted relative to the free organic molecule, confirming the strong N–H$\cdots$X (X = Cl, Br) hydrogen bonding network anchoring the organic and inorganic components.

The C–H asymmetric and symmetric stretching vibrations were detected in the range of 2950–2850 cm^{-1} across all samples, with minor shifts attributable to subtle differences in packing density and halide interactions. In the fingerprint region (1500–1200 cm^{-1}), prominent bands corresponding to C–N stretching and CH_2 bending vibrations were evident. Importantly, the comparison revealed that the C–N stretching band appeared at slightly lower wavenumbers in the $(C_8H_{14}N_2)_2[Bi_2Br_{10}]\cdot 2H_2O$ sample ($\sim$1245 cm^{-1}) than in the chloride-based systems ($\sim$1260 cm^{-1}), suggesting a slightly

more relaxed binding environment around the nitrogen atoms due to the larger bromide ions.

The low-wavenumber region (<400 cm^{-1}) was highly diagnostic of metal–halide vibrations. In $(C_8H_{14}N_2)_2[Bi_2Br_{10}]\cdot 2H_2O$, broad absorptions at 180–220 cm^{-1} were assigned to Bi–Br stretching within the dimeric $[Bi_2Br_{10}]^{4-}$ units, appearing broader and redshifted relative to Bi–Cl and Sb–Cl due to the heavier mass and greater polarizability of bromide ions. In $(C_8H_{14}N_2)_3[BiCl_6]_2$, the Raman spectrum showed no well-defined peaks below 500 cm^{-1}, where Bi–Cl stretches are normally expected, because strong fluorescence masked the signal. Only very weak traces near 270–290 cm^{-1} could be detected after magnification, with intensities too low for reliable interpretation, so this spectrum was only briefly noted to acknowledge fluorescence suppression of Raman activity. In contrast, $(C_8H_{14}N_2)[SbCl_5]$ exhibited clear Sb–Cl stretching bands at 260–275 cm^{-1}, slightly redshifted relative to Bi–Cl in line with weaker Sb–Cl bonds despite similar $Sb3^+$ and $Bi3^+$ radii. A weak, broad feature at $\sim$180 cm^{-1} was also observed, assigned to bending vibrations of the distorted $[SbCl_5]^{2-}$ polyhedra.

The calculated vibrational modes confirmed the assignment of metal–halide stretching, organic skeleton vibrations, and hydrogen bonding signatures. Minor discrepancies between theoretical and experimental frequencies, typically within 20–30 cm^{-1}, were attributed to crystal packing effects, anharmonicities, and limitations of the model clusters.

Comparatively, the vibrational spectral profiles underscored the influence of the halide identity and the metal center on the bonding characteristics of the hybrid structures. The progression from Bi–Br to Bi–Cl to Sb–Cl systems revealed a systematic blue-shift of metal–halide stretching modes, reflecting decreasing mass and bond flexibility. Furthermore, variations in hydrogen bond strengths, as inferred from the N–H stretching region, directly correlated with the halide size and coordination geometry, showcasing the delicate interplay between inorganic framework stiffness and organic cation environment. Thus, FTIR and Raman spectroscopic studies, combined with DFT simulations, provided compelling evidence of the structural distinctiveness of each compound, bridging vibrational fingerprints to the underlying crystallographic and electronic architectures.

3.4. Optical properties and band gap evaluation

3.4.1. UV-vis absorption spectroscopy. The optical absorption behavior of the three hybrid compounds was investigated through UV-Vis spectroscopy, both in solution and in the solid state (except $(C_8H_{14}N_2)[SbCl_5]$, which was investigated only in its solid state) (Fig. 4). For solution-state measurements, the samples were dissolved in suitable solvents under ambient conditions to probe intrinsic optical transitions without solid-state packing effects. Solid-state optical absorption was analyzed *via* diffuse reflectance spectroscopy (DRS), and the data were processed using the Kubelka–Munk transformation to obtain pseudo-absorption profiles.

For $(C_8H_{14}N_2)_2[Bi_2Br_{10}]\cdot 2H_2O$, the solution UV-Vis spectrum displayed a broad absorption band centered around 325–375 nm, attributed to ligand-to-metal charge transfer (LMCT) transitions involving the $[Bi_2Br_{10}]^{4-}$ dimers. In the solid-state DRS spectrum, a pronounced absorption onset was observed

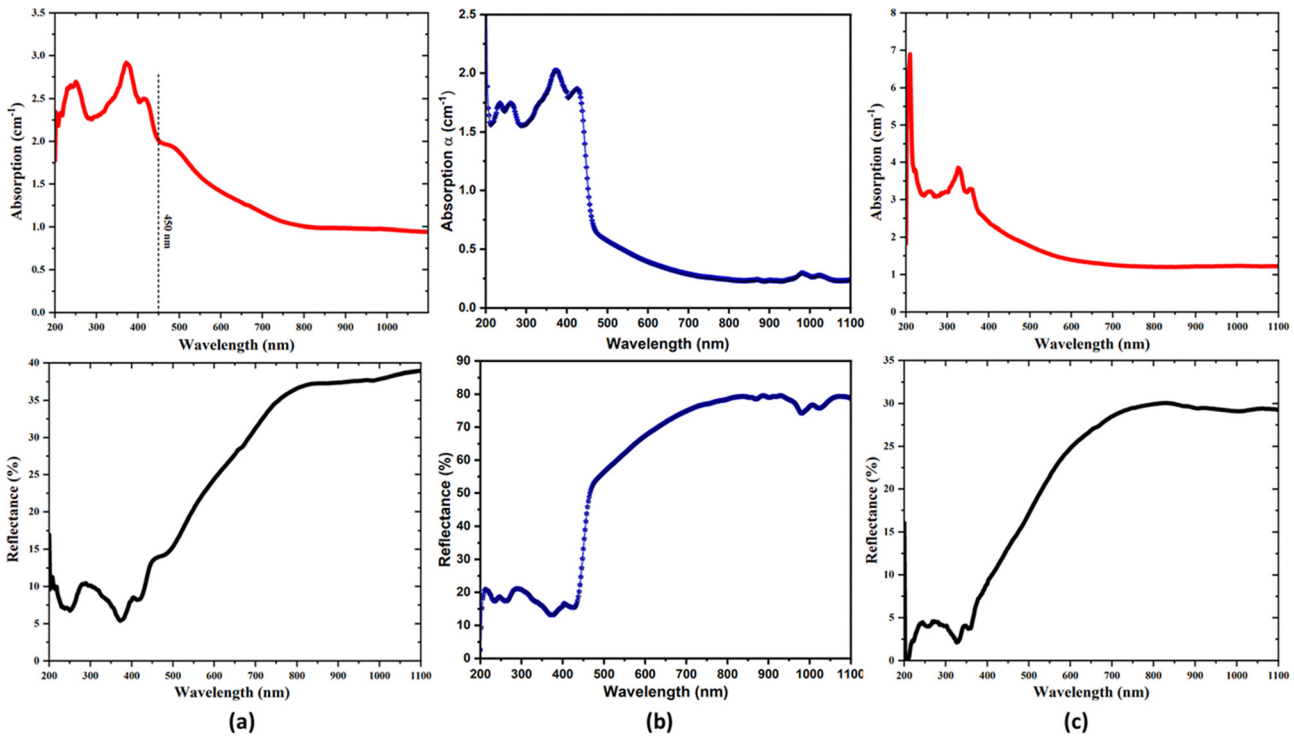

Fig. 4 Comparative UV-vis absorption and reflectance spectra of (a) **M4**, (b) **M41**, and (c) **M43**.

near 440 nm, extending into the visible region, consistent with the bromide's stronger polarizability and the enhanced dimensionality of the dimeric framework. In **M4**, the presence of lattice water introduces an extended hydrogen-bonding network that slightly perturbs the local coordination environment of the $[Bi_2Br_{10}]^{4-}$ units. This hydration-induced structural flexibility can lead to modest shifts in the optical absorption edge and provides additional vibrational relaxation pathways through O–H modes, partially dampening emission intensity relative to the anhydrous analogues. The observed optical behavior is therefore governed by water-mediated structural distortion rather than any intrinsic optical activity of the water molecules.

In the case of $(C_8H_{14}N_2)_3[BiCl_6]_2$, the solution spectrum revealed a narrower absorption band peaking around 290–310 nm, characteristic of LMCT transitions within isolated $[BiCl_6]^{3-}$ octahedra. The solid-state DRS profile showed a sharp absorption edge at approximately 360 nm, indicating a wider optical gap compared to the bromide analogue, as expected from the lighter, less polarizable chloride ligands.

For $(C_8H_{14}N_2)[SbCl_5]$, solid-state measurements exhibited an absorption edge around 450 nm, corresponding to a direct optical gap of ≈2.77 eV. Notably, **M41** presents the smallest gap among the three compounds (**M41** < **M4** < **M43**), despite being chloride-based; within the Bi-series, the absorption onset blue-shifts on going from Br^- to Cl^- (**M4** → **M43**), but substitution of Bi^{3+} → Sb^{3+} modifies the orbital contributions and coordination geometry such that the Sb derivative (**M41**) is red-shifted relative to the BiCl compound.

Overall, the absorption onset systematically blue-shifted from the bromide-based to chloride-based compounds, underscoring the effect of halide type and metal center on the optical absorption properties.

3.4.2. Band gap determination (Tauc and TD-DFT). The optical band gaps of the compounds were estimated using Tauc plots derived from the solid-state diffuse reflectance data,[31,32] and confirmed based on structural considerations and theoretical calculations (Fig. 5 and 7).

For $(C_8H_{14}N_2)_2[Bi_2Br_{10}]\cdot 2H_2O$, the Tauc plot based on Kubelka–Munk-transformed diffuse reflectance data clearly confirms an indirect band gap nature, with the extrapolated value yielding $E_g \approx 2.9$ eV, consistent with the absorption onset at ∼440 nm. This assignment is strongly supported by the logarithmic slope analysis ($n \approx 2$), photoluminescence characteristics showing phonon-assisted recombination with a red-shifted emission at 706 nm, and TD-DFT density of states (DOS) calculations, which corroborated the experimental value, predicting the first allowed transition near 2.85 eV, predominantly involving Br p-orbital to Bi 6p-orbital transitions, all of which confirm the indirect nature of the transition.

For $(C_8H_{14}N_2)_3[BiCl_6]_2$, the Tauc analysis of the DRS spectrum confirms an indirect allowed transition, yielding a band gap of approximately 3.16 eV. This value matches well with the second derivative and computational DOS analysis (E_g = 3.1 eV), which supports the indirect nature of the transition, consistent with a charge transfer process from Cl 3p to Bi 6p orbitals.

In contrast, $(C_8H_{14}N_2)[SbCl_5]$ exhibits a well-defined direct optical band gap of 2.77 eV, as established through both the $(F(R)h\nu)^2$ Tauc plot and sharp absorption edge at ∼450 nm. Theoretical calculations reinforce this direct nature with a HOMO–LUMO gap of 2.7 eV. This implies a momentum-conserving transition with efficient radiative recombination, attributed to Cl 3p → Sb 5p charge transfer mechanisms.

Thus, both experimental and theoretical results confirm a consistent structure–optical property relationship across the three compounds: the band gap widens with halide substitution from Br^- to Cl^-, and narrows again upon replacing Bi^{3+} with Sb^{3+}, while the band structure shifts from indirect in the Bi-based compounds to direct in the Sb-based system, a trend rooted in orbital overlaps and coordination symmetry within the hybrid frameworks.

3.4.3. Photoluminescence and chromaticity analysis. Photoluminescence (PL) studies were conducted for all three hybrid halometallate compounds, $(C_8H_{14}N_2)_2[Bi_2Br_{10}]\cdot 2H_2O$, $(C_8H_{14}N_2)[SbCl_5]$, and $(C_8H_{14}N_2)_3[BiCl_6]_2$, to investigate their emission properties under UV excitation (Fig. 6). Among them, $(C_8H_{14}N_2)_2[Bi_2Br_{10}]\cdot 2H_2O$ exhibited the most pronounced and complex PL behavior, displaying both broad emission around 645 nm under excitation at 319 nm, and a sharp peak at 706 nm under excitation at 350 nm, characteristic of phonon-assisted recombination and an indirect bandgap. The emission is attributed to charge carrier relaxation within the distorted

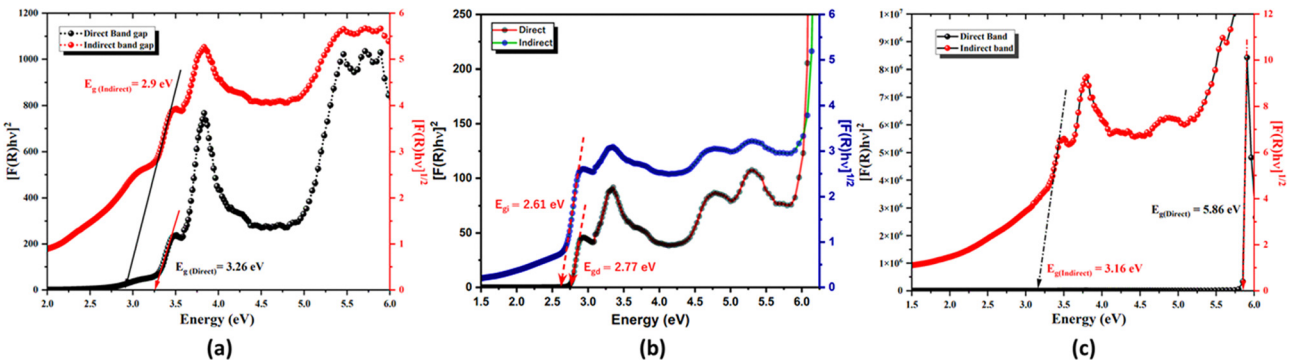

Fig. 5 Band gap determination of compounds: (a) **M4**, (b) **M41**, and (c) **M43**, *via* Tauc plots from DRS (Kubelka–Munk Function).

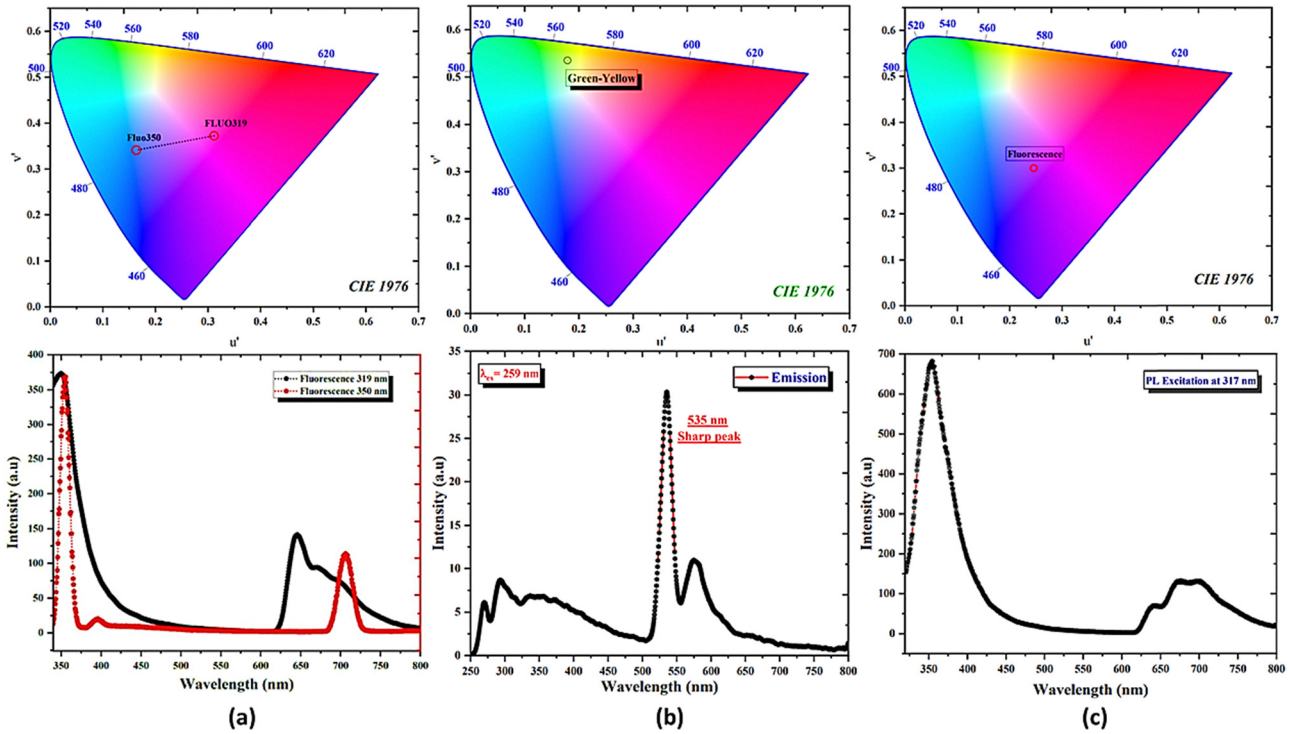

Fig. 6 Photoluminescence emission spectra and CIE chromaticity mapping comparison of compounds: (a) **M4**, (b) **M41**, and (c) **M43**.

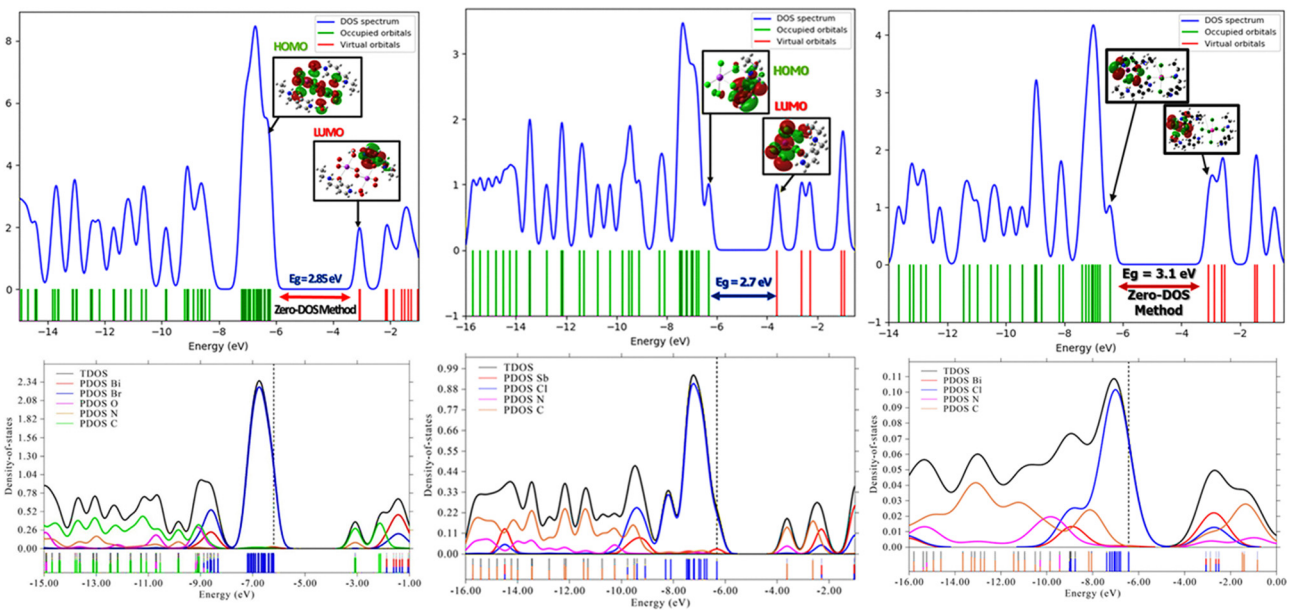

Fig. 7 Density of states (DOS) and projected density of states (PDOS) analysis of compounds: (a) **M4**, (b) **M41**, and (c) **M43**.

$[Bi_2Br_{10}]^{4-}$ sublattice, involving exciton dynamics and self-trapping effects. Chromaticity analysis using the CIE 1976 (u', v') diagram revealed excitation-dependent emission, with coordinates shifting from (u' = 0.311, v' = 0.371) at 319 nm to (u' = 0.164, v' = 0.344) at 350 nm, demonstrating tunability across the rose to cyan-blue region. In contrast, $(C_8H_{14}N_2)[SbCl_5]$ exhibited a prominent emission peak at 571 nm under 259 nm excitation, with additional broad features spanning 250–800 nm, suggesting contributions from both band-to-band and defect-assisted transitions. Its chromaticity coordinates (u' = 0.179, v' = 0.535) position the emission in the green-yellow region. For $(C_8H_{14}N_2)_3[BiCl_6]_2$, a strong emission centered at 353 nm was observed, aligning with its bandgap energy of 3.39 eV, indicating efficient radiative recombination likely

enhanced by localized states despite its indirect gap. The emission's chromaticity coordinates confirm UV-region output, consistent with potential application in UV-emitting or down-conversion photonic devices. These PL results underscore the influence of halide identity, metal center, and structural dimensionality on emission efficiency, spectral position, and potential optoelectronic application of these materials.

The photoluminescence behavior of these compounds reveals the critical influence of halide identity and metal center on optical performance, despite all three sharing the same organic cation $(C_8H_{14}N_2)^{2+}$. The bromide-based bismuth compound, $(C_8H_{14}N_2)_2[Bi_2Br_{10}]\cdot 2H_2O$, exhibits the most complex and intense emission profile, with both broad and sharp features indicative of both strong high-energy excitonic coupling processes and low-energy phonon-assisted recombination or self-trapped exciton dynamics, which is typical of indirect bandgap systems with strong spin–orbit coupling, and a hallmark of distorted Bi–Br frameworks with strong spin–orbit coupling and dimeric $[Bi_2Br_{10}]^{4-}$ substructures. In contrast, $(C_8H_{14}N_2)_3[BiCl_6]_2$ emits in the UV with a narrow peak at 353 nm, showing limited defect-mediated processes and reinforcing its potential as a UV emitter. In this case, replacing Br with Cl in the Bi-based system, $(C_8H_{14}N_2)_3[BiCl_6]_2$, leads to a significantly blue-shifted and sharper UV emission at 353 nm, suggesting a more rigid lattice and reduced phonon interactions, with minimal defect-mediated recombination. The Sb-based analogue, $(C_8H_{14}N_2)[SbCl_5]$, while also chloride-based, demonstrates an intermediate behavior: a prominent emission at 571 nm, indicative of a potentially more direct transition facilitated by weaker spin–orbit coupling in Sb^{3+} compared to Bi^{3+}, along with greater structural asymmetry. These results underscore how systematic substitution of halogen (Cl *vs.* Br) and metal (Bi *vs.* Sb), while keeping the organic component constant, allows fine control over band structure, exciton localization, and emission properties, offering a modular design approach for tuning photophysical responses in hybrid halometallates.

The contrast between the pronounced broadband PL of **M4** and the suppressed emission of **M43** arises from the combined influence of halide identity and local anionic topology. In **M4**, the large, highly polarizable Br^- ions produce broader Br 4p-derived valence bands and enhanced halide–metal orbital overlap, while the dimeric $[Bi_2Br_{10}]^{4-}$ connectivity and lattice water induce local structural flexibility that favors exciton self-trapping and phonon-assisted radiative recombination. Conversely, the smaller, less polarizable Cl^- yields sharper, more localized valence bands, and in **M43** the isolated $[BiCl_6]^{3-}$ units are embedded in a rigid hydrogen-bonded matrix that suppresses STE formation and quenches broadband PL.

3.5. Theoretical insights into electronic structure

To complement and rationalize the experimental findings, density functional theory (DFT) and time-dependent DFT (TD-DFT) calculations were performed on representative molecular clusters derived from the crystallographic structures of the three compounds. A comprehensive analysis of frontier molecular orbitals (FMOs), density of states (DOS and PDOS) (Fig. 7), electrostatic potential (ESP) maps, electron localization function (ELF), localized orbital locator (LOL), and reduced density gradient (RDG) non-covalent interaction plots was conducted to elucidate the electronic distributions, bonding characteristics, and the nature of intermolecular forces governing their semiconducting behavior.

3.5.1. Analysis of Frontier molecular orbitals, band gaps, and density of states (DOS and PDOS). For $(C_8H_{14}N_2)_2[Bi_2Br_{10}]\cdot 2H_2O$, the HOMO was mainly localized on the bromide ligands within the dimeric $[Bi_2Br_{10}]^{4-}$ unit, with secondary contributions from Bi 6s and 6p orbitals. The LUMO was centered predominantly on the Bi atoms, indicating a ligand-to-metal charge transfer (LMCT) characteristic. The calculated HOMO–LUMO gap was 2.85 eV, closely matching the experimental optical band gap of 2.9 eV, confirming the material's semiconducting nature and validating the accuracy of the theoretical model.

In the case of $(C_8H_{14}N_2)_3[BiCl_6]_2$, a comparable orbital distribution was observed, with the HOMO localized on the chloride p orbitals and the LUMO concentrated on Bi 6p orbitals. Due to the smaller size and lower polarizability of Cl^- ions compared to Br^-, the HOMO energy was further stabilized, resulting in a larger HOMO–LUMO gap of 3.1 eV, in close agreement with the experimentally determined optical gap of 3.16 eV.

For $(C_8H_{14}N_2)[SbCl_5]$, the HOMO was primarily distributed across the chloride ligands surrounding the Sb^{3+} center, while the LUMO was located on the Sb 5p orbitals. The theoretical HOMO–LUMO energy gap was estimated at 2.7 eV, again closely aligning with the measured experimental band gap of 2.77 eV. The substitution of Bi^{3+} by Sb^{3+} in this compound introduced subtle variations in orbital energies and electronic distributions, reflecting differences in electronegativity and bonding interactions within the $[SbCl_5]^{2-}$ unit.

Collectively, the nature and spatial distribution of the FMOs in all three compounds support the assignment of their primary electronic transitions as LMCT in nature. These results further confirm the semiconducting behavior and validate the indirect band gap characteristics observed experimentally.

Additionally, the total and partial density of states (DOS and PDOS) analyses provided further insight into the electronic structure. In all three cases, the valence band maximum (VBM) was dominated by halide p orbitals (Br 4p or Cl 3p), whereas the conduction band minimum (CBM) was composed primarily of the metal p orbitals (Bi 6p or Sb 5p). Notably, $(C_8H_{14}N_2)_2[Bi_2Br_{10}]\cdot 2H_2O$ displayed a broader valence band profile, indicative of greater orbital overlap and enhanced electronic delocalization due to the higher polarizability and larger size of Br^- ions. In contrast, the chloride-based compounds, $(C_8H_{14}N_2)_3[BiCl_6]_2$ and $(C_8H_{14}N_2)[SbCl_5]$, exhibited sharper valence band features, suggesting more localized charge distributions. Minor differences in CBM energy levels between the Bi–Cl and Sb–Cl systems were attributed to distinct metal–ligand hybridizations and orbital contributions.

The broader halide-derived valence band in **M4** (Fig. 7(a)) directly correlates with the observed broadband, self-trapped-

exciton emission, whereas the sharper Cl-derived valence bands in **M43** (Fig. 7(c)) signal stronger localization and fewer emissive STE pathways.

The difference between the indirect band gaps of the Bi-based compounds and the direct gap of the Sb-based analogue arises primarily from the much stronger spin–orbit coupling (SOC) associated with Bi^{3+}. The relativistic SOC interaction significantly perturbs and splits the Bi-6p conduction-band states, shifting the conduction-band minimum to a *k*-point different from that of the valence-band maximum and thus yielding an indirect transition. In contrast, Sb^{3+} exhibits substantially weaker SOC, leading to less perturbation of its 5p-derived conduction band and preserving a direct VBM–CBM alignment. DOS and PDOS analyses, while confirming the dominant halide-p and metal-p contributions, cannot directly reveal the direct/indirect nature, which strictly requires periodic band-structure calculations. Although such $E(k)$ computations are beyond the capabilities of Gaussian, future work using periodic DFT (*e.g.*, VASP or Quantum Espresso) will be undertaken to explicitly map the dispersion and SOC effects.

3.5.2. Molecular electrostatic potential (ESP) maps. Molecular electrostatic potential (ESP) maps were constructed to visualize the surface charge distribution and potential reactive sites (Fig. 8).

For $(C_8H_{14}N_2)_2[Bi_2Br_{10}]\cdot 2H_2O$, the ESP surface displayed strongly negative potential regions localized over the terminal and bridging bromide atoms, while the positive regions were centered on the protonated nitrogen atoms of the organic moiety. This pronounced polarity facilitates strong hydrogen bonding interactions, as evidenced in the crystal packing.

Similar ESP distributions were observed in $(C_8H_{14}N_2)_3[BiCl_6]_2$ and $(C_8H_{14}N_2)[SbCl_5]$, although the magnitude of negative potential over the chloride atoms was slightly lower compared to bromide ions, consistent with chloride's smaller size and lower polarizability. This reduced surface negativity correlates with the tighter hydrogen bonding and denser packing observed in the chloride structures.

3.5.3. Electron localization function (ELF) and localized orbital locator (LOL). The ELF and LOL mappings (Fig. 9) revealed key features of electron pair localization within the inorganic frameworks. In all three compounds, high ELF values were concentrated around the halide ions, signifying the presence of strongly localized lone pairs. In contrast, the metal centers (Bi^{3+} or Sb^{3+}) displayed low ELF values, indicating their role as electron acceptors in the LMCT transitions.

Notably, in $(C_8H_{14}N_2)[SbCl_5]$, the ELF plots exhibited more asymmetric distributions around the Sb centers compared to Bi centers, suggesting greater lone pair activity in the Sb coordination environment, in agreement with the structural observations from SCXRD.

The LOL plots confirmed these findings, clearly illustrating the localization of bonding and non-bonding electron density in the hybrid systems and highlighting the influence of halide type and metal identity on the electronic distribution.

3.5.4. Non-covalent interaction analysis (NCI-RDG). Non-covalent interaction (NCI) analyses (Fig. 10), based on reduced density gradient (RDG) functions, were employed to visualize weak interactions stabilizing the crystal structures.

In $(C_8H_{14}N_2)_2[Bi_2Br_{10}]\cdot 2H_2O$, RDG isosurfaces revealed extensive green regions between the organic cations and bromide ions, corresponding to strong N–H···Br hydrogen bonds, as well as weak van der Waals contacts. Blue regions indicated strong, highly attractive interactions within the hydrogen bond network.

For $(C_8H_{14}N_2)_3[BiCl_6]_2$ and $(C_8H_{14}N_2)[SbCl_5]$, the RDG maps showed similar interaction patterns, though slightly less extensive in spatial distribution, reflecting the shorter, stronger, and more localized N–H···Cl hydrogen bonds compared to their Br counterparts. Weak dispersion interactions between adjacent organic moieties were also detected.

The comparative NCI-RDG plots thus highlighted that while all three structures are primarily stabilized by strong hydrogen bonds, the strength, extent, and delocalization of these interactions are finely tuned by the halogen species and the metal center involved.

3.6. Electrochemical properties

Electrochemical impedance spectroscopy (EIS) measurements were exclusively carried out on the $(C_8H_{14}N_2)[SbCl_5]$ compound to explore its dielectric relaxation dynamics and charge transport properties under varying thermal conditions. The experiments were conducted over a wide frequency range (40 Hz to 10^7 Hz) and within a temperature window spanning 313 K to 413 K, enabling detailed analysis of both bulk and interfacial

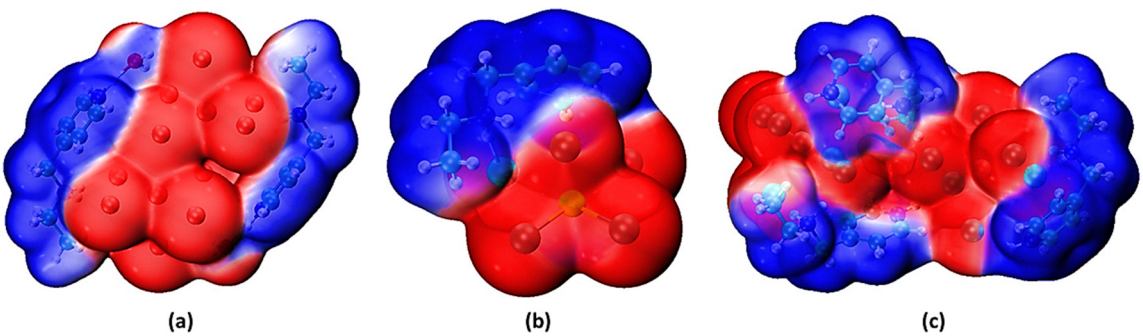

Fig. 8 Molecular electrostatic potential (ESP) maps of compounds: (a) **M4**, (b) **M41**, and (c) **M43**.

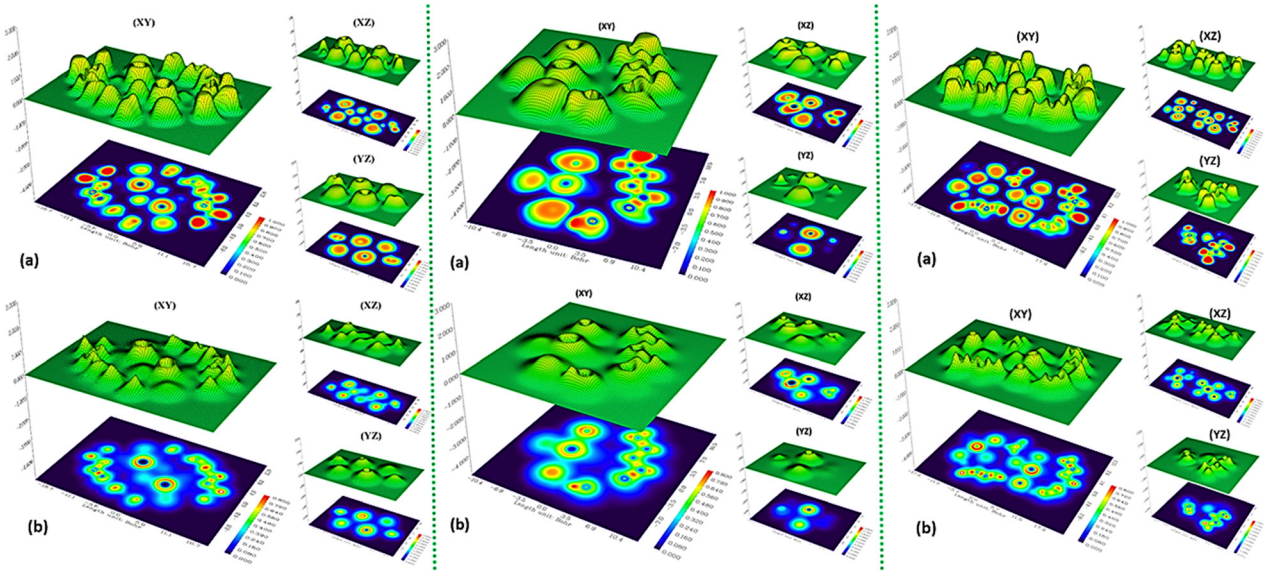

Fig. 9 Electron localization function (ELF) and localized orbital locator (LOL) analyses of compounds: (a) **M4**, (b) **M41**, and (c) **M43**.

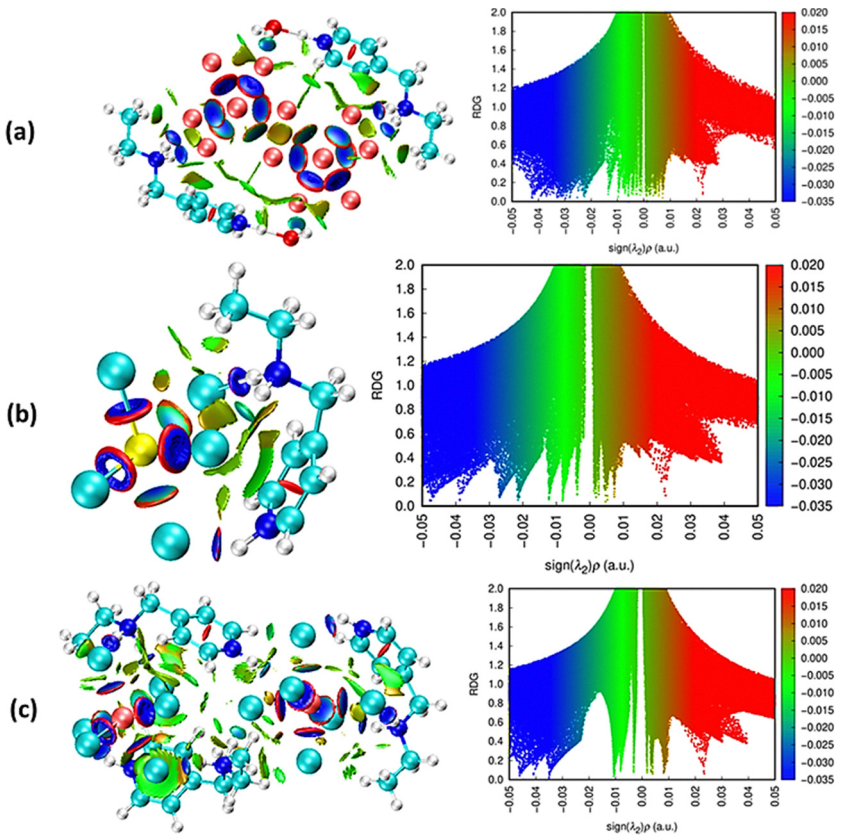

Fig. 10 Non-covalent interaction (NCI) analysis *via* RDG isosurfaces for compounds: (a) **M4**, (b) **M41**, and (c) **M43**.

phenomena. Electrochemical impedance spectroscopy (EIS) was performed exclusively for **M41** because, among the three materials, only the Sb–Cl compound presents structural features that render ionic mobility plausible. In halometallate hybrids, significant ionic transport typically requires either extended dimensionality or the presence of small, mobile carriers. **M41** contains relatively small Cl^- ions within a compact 0D framework that shows measurable lability in solution, making it a reasonable candidate for conductivity studies. In contrast, **M4** is built from a heavy dimeric $[Bi_2Br_{10}]^{4-}$ unit

containing larger bromide ions with limited mobility, while **M43** features rigid isolated $[BiCl_6]^{3-}$ octahedra with no viable migration pathways. Moreover, the structural water present in **M4** would artificially inflate the conductivity through transient protonic contributions, yielding non-reproducible and humidity-dependent values. For these reasons, EIS measurements for **M4** and **M43** were not pursued, as negligible and non-intrinsic conductivities were expected.

The Nyquist plots (Z'' *vs.* Z') across the investigated temperatures exhibited typical depressed semicircular arcs, characteristic of non-ideal Debye relaxation, followed by an inclined tail at low frequencies due to electrode polarization effects (Fig. S5). Equivalent circuit modeling revealed a complex network involving a series resistor and inductor (Rs–L_1), followed by two parallel R–CPE elements, accurately capturing the contributions from bulk grains and grain boundaries. As the temperature increased, a systematic decrease in the arc diameter was observed, consistent with a thermally activated conduction mechanism. However, discrete jumps in the arc size indicated that phase transitions were occurring, confirmed by complementary thermal analysis. The bulk resistance (Rb), extracted from the high-frequency intercept, decreased markedly with temperature, demonstrating enhanced charge carrier mobility.

The direct current conductivity (σ_{dc}) (Fig. S6), calculated using the relationship $\sigma_{dc} = L/(R{\cdot}A)$, followed an Arrhenius-type dependence, with a notable deviation at phase boundaries. Linear fitting of the $\ln(\sigma T)$ *versus* $1000/T$ plot yielded two distinct activation energies: E_{a1} = 0.39 eV for the lower-temperature phase (323–353 K) and E_{a2} = 0.97 eV for the higher-temperature phase (363–403 K). The relatively low E_{a1} value suggests a moderate ionic or polaronic hopping conduction mechanism in the low-temperature crystalline phase, comparable to many hybrid halide and low-dimensional materials. In contrast, the substantially higher E_{a2} indicates a significant increase in transport barriers, likely driven by lattice rearrangements, enhanced localization of charge carriers, or deeper trap state formation upon phase transition.

The modulus spectroscopy (M' and M'') analysis (Fig. S7) further supported these findings. Relaxation peaks in M'' shifted systematically toward higher frequencies with increasing temperature, reflecting a decrease in relaxation time (τ) and confirming thermally activated short-range carrier motion. The non-ideal broadness of these peaks suggested a distribution of relaxation times, highlighting structural heterogeneity within the hybrid matrix.

Overall, the EIS analysis revealed that $(C_8H_{14}N_2)[SbCl_5]$ exhibits a complex temperature-dependent dielectric behavior, marked by multiple conduction regimes and phase-transition-driven conductivity modulation, making it a promising candidate for applications in temperature-tunable ionic conductors and hybrid electronic devices.

3.7. Antibiological activity evaluation

The antibacterial activity of the three hybrid halometallates **M4**, **M41**, and **M43** was evaluated alongside their common organic cation and the reference aminoglycoside gentamicin (G) using the agar-well diffusion method (Fig. 11). All hybrid compounds

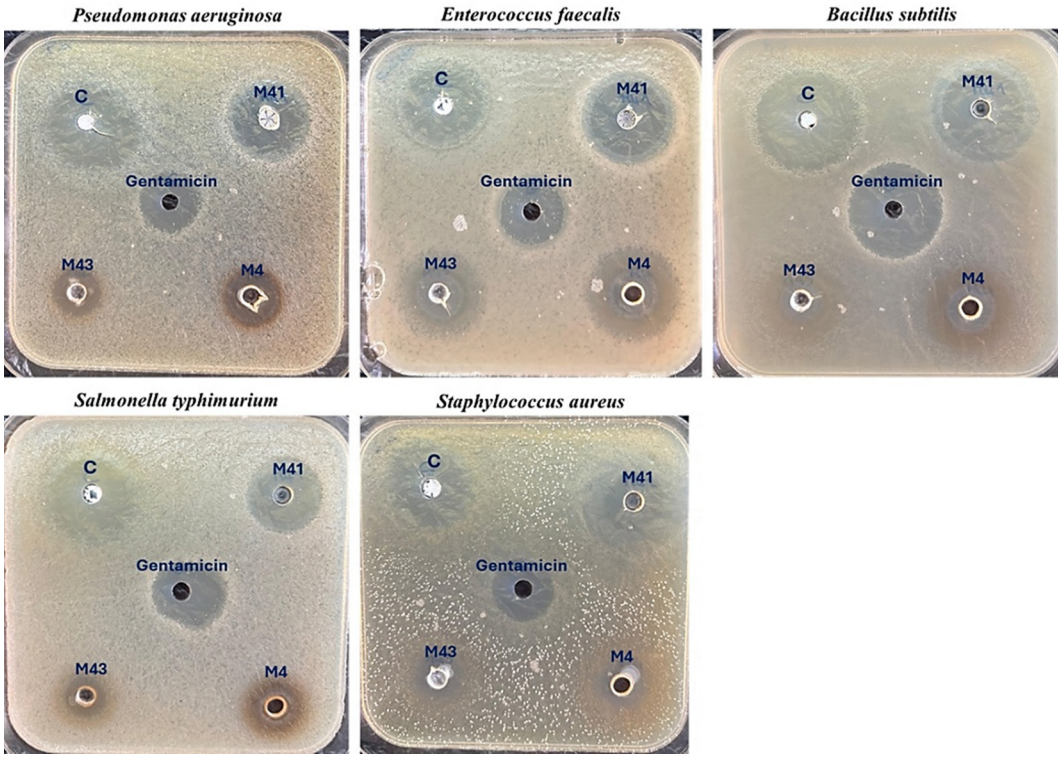

Fig. 11 Antibacterial activity of compounds **M4**, **M41**, and **M43** against Gram-negative (*Pseudomonas aeruginosa*, *Salmonella typhimurium*) and Gram-positive (*Enterococcus faecalis*, *Bacillus subtilis*, *Staphylococcus aureus*) strains.

and the free cation were tested at a concentration of 1 mg mL^{-1} in DMSO, while gentamicin was applied at 15 μg $well^{-1}$. The resulting inhibition zone diameters against five representative bacterial strains, *Pseudomonas aeruginosa* and *Salmonella typhimurium* (Gram-negative), and *Enterococcus faecalis*, *Bacillus subtilis*, and *Staphylococcus aureus* (Gram-positive), are summarized in Table 2. The results reveal a clear dependence of antibacterial performance on both the physicochemical nature of the inorganic framework and the associated ionic dissociation behavior.

The organic aromatic cation exhibits the highest antibacterial activity among all tested species, producing inhibition zones ranging from 29 to 36 mm across all strains. These values exceed those obtained for gentamicin (21–30 mm) and remain relatively uniform for both Gram-positive and Gram-negative bacteria, indicating a broad-spectrum mode of action. Such behavior suggests a mechanism that is not strongly dependent on cell wall architecture and may involve membrane-level interactions or strong electrostatic affinity toward negatively charged bacterial surfaces, potentially facilitated by the amphiphilic character of the cation.

When incorporated into hybrid frameworks, the antibacterial efficacy of the cation becomes strongly modulated by the nature of the inorganic anion and crystal packing. Among the three hybrid materials, **M41** displays the most pronounced antibacterial activity, with inhibition zones ranging from 25 to 34 mm. These values surpass those of gentamicin in four of the five tested strains and match it in the remaining case, demonstrating that the $[SbCl_5]^{2-}$-based lattice allows sufficient dissociation in aqueous media to enable effective release and diffusion of the biologically active cation. The slightly reduced inhibition zones compared to the free cation are reasonably attributed to partial ion pairing and diffusion constraints imposed by the crystalline lattice, without fundamentally suppressing antibacterial potency.

Crystallographic analysis provides insight into the superior performance of **M41**. The anionic component adopts a near-ideal square-pyramidal $SbCl_5$ coordination geometry with relatively short Sb–Cl bond lengths and a highly anisotropic electrostatic potential distribution concentrated along terminal chloride ligands. This configuration favors water-mediated perturbation of the coordination sphere while preserving overall lattice integrity. The packing arrangement of **M41** further reveals moderate density and the presence of accessible interstitial regions between polyhedra, which collectively enhance ionic mobility and diffusion through the solid matrix. The antibacterial activity of **M41** therefore emerges from a synergistic interplay between cation structure, anion geometry, and supramolecular organization, rather than from the intrinsic activity of any single component alone.

Table 2 Summary of antibacterial activities of compounds **M4**, **M41**, and **M43** and their common organic cation against Gram-negative and Gram-positive strains

	Inhibition zone (mm) for				
Bacteria	**M4**	**M41**	**M43**	Cation	G
Pseudomonas aeruginosa	17	29	16	34	21
Enterococcus faecalis	30	31	27	29	25
Bacillus subtilis	26	34	20	36	30
Salmonella typhimurium	19	25	0	32	25
Staphylococcus aureus	15	27	12	30	23

Although hydrogen bonds do not exhibit intrinsic antibacterial activity, their presence enhances framework cohesion and surface polarity, facilitating interfacial interactions between the hybrid material and bacterial membranes. Moreover, hydrogen-bond networks can assist limited solvation and diffusion of active ionic species, indirectly contributing to the observed antibacterial performance.

Mechanistic interpretation of the antibacterial activity, particularly for **M41**, must be considered as a plausible hypothesis supported by indirect evidence rather than direct confirmation. In addition to the structural lability expected for Sb–Cl halometallates, comparative UV-Vis measurements performed for the three compounds under identical aqueous-solution conditions show that **M41** undergoes the greatest spectral changes upon dissolution, whereas the Bi-based analogues (**M4** and **M43**) exhibit much more stable absorption profiles (Fig. S8). This sensitivity of **M41** to the aqueous environment suggests a higher susceptibility to solvation-assisted perturbation of the Sb–Cl coordination sphere and raises the possibility of partial release of cationic or halometallate fragments during biological testing. Such behavior is frequently reported for 0D halometallates and aligns with literature mechanisms involving ion release or fragment-mediated interactions with bacterial membranes. However, definitive mechanistic confirmation would require ion-release quantification (*e.g.*, ICP-OES), membrane-disruption assays, or ROS analyses, which are not currently available in our laboratory. This limitation is now explicitly acknowledged, and future work will aim to directly probe the species present in solution and their interactions with bacterial cells.

In contrast to **M41**, both **M4** and **M43** exhibit significantly reduced antibacterial activity, with inhibition zones decreasing sharply and, in some cases, disappearing entirely. This behavior is consistent with their more compact and strongly bound Bi-based frameworks, which limit ion mobility and hinder the release of biologically active species. In **M4**, the dimeric $[Bi_2Br_{10}]^{4-}$ anion forms a heavy, highly polarizable cluster that promotes strong ion pairing and kinetically suppresses cation liberation. Similarly, the presence of two $[BiCl_6]^{3-}$ units in **M43** contributes to a rigid and densely packed lattice that further restricts diffusion.

Although water itself does not exhibit antibacterial activity, the lattice water present in **M4** can indirectly influence biological performance by increasing local framework flexibility and facilitating limited solvation-assisted mobility of metal-containing species. This effect may enhance interfacial interactions with bacterial membranes and contribute to antibacterial activity that is stronger than that of the fully anhydrous Bi–Cl analogue (**M43**), though still weaker than the Sb–Cl compound (**M41**), which benefits from intrinsically higher ionic lability.

The superior antibacterial performance of **M41** can be rationalized in terms of its crystallographic and electronic characteristics. With a nearly ideal square-pyramidal $SbCl_5$ geometry and a high packing efficiency of 92.9%, the lattice strikes a balance between structural integrity and sufficient void accessibility (7.1%), enabling effective dissociation and release of the biologically active cation. This contrasts with the denser Bi_2Br_{10} framework of **M4**, where strong ion pairing suppresses cation mobility, and with the moderately distorted $BiCl_6$ network of **M43**, where lattice disorder hampers uniform release. The correlation between packing density, electrostatic potential distribution, and cation availability thus explains why **M41** consistently outperforms gentamicin across multiple bacterial strains. Importantly, this activity is preserved against both Gram-positive and Gram-negative bacteria, suggesting that the amphiphilic cation circumvents permeability barriers and operates *via* membrane-level interactions, offering a potential route to overcoming resistance mechanisms that typically limit the efficacy of conventional antibiotics.

Comparable antibacterial performance has been reported for halobismuthate hybrids in recent studies. Ouerghi *et al.*[33] investigated the chlorobismuthate $(C_6H_7NCl)_3[BiCl_6]\cdot H_2O$, which under a disk diffusion assay (100 μg per disc) produced inhibition zones of ~12 mm against *Escherichia coli* and ~9 mm against *Pseudomonas aeruginosa*, reflecting a moderate release of cationic species from the lattice. Ben Ali *et al.*[34] examined the tetraiodobismuthate $(H_2DDS)[Bi_4I_{16}]$, tested by agar-well diffusion at 1 mg per well, and reported inhibition zones of 11 ± 1.4 mm (*E. coli*) and 8 mm (*P. aeruginosa*), highlighting the critical influence of halide identity and counterion chemistry on antibacterial efficacy. In contrast, the present Sb–Cl hybrid (**M41**) exhibits markedly superior inhibition zones ranging from 25 to 34 mm across the tested strains, while its free organic cation achieves 29–36 mm under identical assay conditions (1 mg per well). These results clearly demonstrate that both the organic cation and the hybrid lattice synergistically amplify antimicrobial potency, surpassing comparable halobismuthate frameworks even under equivalent or more stringent loading conditions. For reference, the standard antibiotic gentamicin (15 μg per well) typically produces inhibition zones of 21–30 mm, placing **M41** at or above clinically relevant levels of antibacterial performance. A comparison of the common tests for these two compounds *vs*. our **M41** and the free cation is shown in Table S2.

Theoretical hydration models would predict that Cl^-, being smaller and less polarizable than Br^-, generates a more dynamic hydration sphere, lowering the energetic barrier for dissociation and enabling faster pharmacologically relevant ion release. Moreover, Sb(III) occupies a position of intermediate hardness in Pearson's HSAB classification, allowing selective reactivity toward biomolecular targets without over-stabilization of the lattice, in contrast to the stronger lattice retention observed with Bi(III) bromide systems. This combination of geometric efficiency, balanced bond enthalpy, and favorable hydration thermodynamics positions **M41** as a highly effective cation delivery scaffold. At the molecular level, the cation-bearing π–π stacking capability from its aromatic rings, hydrogen-bond donor/acceptor functionality, and hydrophobic patches interact synergistically with bacterial membranes, potentially inserting into lipid bilayers and disrupting membrane integrity while engaging in electrostatic attraction to negatively charged bacterial surfaces. The superior performance of **M41** relative to G may thus be traced to a dual mechanism: the intrinsic bioactivity of the cation and a lattice-enabled kinetic release pathway that amplifies its biological impact.

Beyond the immediate antibacterial assays, these findings carry broader implications for the rational design of crystalline salt-based antimicrobials. One can envision tailoring polyhedral anionic geometries, packing arrangements, and ion-pair polarity to tune dissolution rates, membrane affinity, and strain selectivity for applications in antimicrobial coatings, slow-release wound dressings, and targeted drug delivery platforms.

From a theoretical perspective, these structure–activity relationships evidenced here suggest that subtle adjustments in anion size, charge distribution, and coordination geometry could be computationally optimized, inviting a multipronged modeling approach to rationalize and predict bioactivity, using Quantum mechanical calculations, for example, density functional theory (DFT) to estimate lattice energies, hydration free energies, and ion-pair binding affinities, and molecular dynamics (MD) to simulate cation–membrane interactions, yielding predictive control over pharmacological performance. Quantum mechanical calculations (*e.g.*, DFT) could quantify ion-pair dissociation energies, frontier orbital distributions, and electrostatic potential maps, elucidating why **M41** permits greater cation liberation than **M4** or **M43**. Molecular dynamics simulations in explicit bacterial membrane models could probe the adsorption kinetics, insertion depth, and perturbation energy of the cation, while docking studies against model bacterial enzymes or nucleic acid structures could reveal secondary binding modes. Solvation thermodynamics and log*P* calculations would help correlate hydrophilicity/hydrophobicity balances to observed agar diffusion radii. Such computational–experimental integration could lead to predictive structure–activity relationships, guiding the design of next-generation cation–anion frameworks with optimized solubility, release kinetics, and membrane targeting capabilities. Beyond antibacterial applications, the strong cationic amphiphilicity suggests potential utility in biofilm disruption, synergistic antibiotic combinations (especially with cell wall–targeting agents), and surface coatings for medical devices to prevent microbial colonization. In sum, this study not only identifies the organic cation and **M41** as high-potency, broad-spectrum antibacterial candidates but also establishes a mechanistic and theoretical foundation for the rational engineering of hybrid halometallate antimicrobials that can rival, and in some cases surpass, the performance of established clinical drugs like gentamicin, with promising implications for combating multidrug-resistant pathogens. Therefore, **M41** stands as both a proof-of-concept and a blueprint for integrating crystallographic precision with biochemical targeting, bridging solid-state chemistry with applied biomedical functionality in a way that surpasses conventional small-molecule antibacterial agents like G.

3.8. Structure–property–function correlation

The comprehensive comparative analysis of $(C_8H_{14}N_2)_2[Bi_2Br_{10}]\cdot 2H_2O$, $(C_8H_{14}N_2)_3[BiCl_6]_2$, and $(C_8H_{14}N_2)[SbCl_5]$ reveals a nuanced interplay between crystal structure, bonding motifs, and the resulting optical, electronic, and dielectric behaviors. Despite all three compounds exhibiting a 0D metal–halide coordination core, distinct differences in halide identity, metal center, local geometric distortion, and supramolecular organization critically govern their divergent functionalities.

The bromide-based $(C_8H_{14}N_2)_2[Bi_2Br_{10}]\cdot 2H_2O$ crystallizes in the monoclinic $P2_1/c$ space group and features centrosymmetric dimeric $[Bi_2Br_{10}]^{4-}$ units interconnected by two μ_2-bridging bromides. The larger ionic radius and higher polarizability of Br^- compared to Cl^- produce longer Bi–Br bonds and greater polyhedral flexibility, favoring exciton localization and the formation of self-trapped excitons (STEs). This behavior is reflected in its prominent broadband photoluminescence centered near 470 nm and a relatively narrow experimental optical band gap of 2.90 eV, closely supported by the theoretical HOMO–LUMO value of 2.85 eV. Density of states (DOS) calculations reveal broader Br 4p-derived valence bands, confirming enhanced electronic delocalization through the polarizable Bi–Br framework. Moreover, the presence of two lattice water molecules expands the hydrogen-bonding network, contributing to framework softness while maintaining the highest packing efficiency of the series at 94.1% (5.9% void), as established by X-ray analysis. The dense yet flexible bromide lattice combines robustness with strong emissive behavior, rendering $(C_8H_{14}N_2)_2[Bi_2Br_{10}]\cdot 2H_2O$ a promising candidate for broadband optoelectronic applications.

In contrast, $(C_8H_{14}N_2)_3[BiCl_6]_2$ adopts the triclinic $P\bar{1}$ space group and consists of isolated $[BiCl_6]^{3-}$ octahedra embedded within a three-dimensional hydrogen-bonded matrix. The substitution of Br^- with the smaller and less polarizable Cl^- ions, combined with the absence of lattice water, results in shorter Bi–Cl bonds but also the highest octahedral distortion among the three compounds. This distortion, together with its lower packing efficiency, disrupts exciton self-trapping pathways and suppresses photoluminescence. The compound exhibits the widest experimental band gap of 3.16 eV, closely matching the theoretical value of 3.1 eV, reflecting its electronic localization and optical transparency. Hirshfeld surface analysis and interaction energy topology confirm the rigidity of its hydrogen-bonding framework, which reduces charge transport and favors insulating behavior. Consequently, $(C_8H_{14}N_2)_3[BiCl_6]_2$ is structurally optimized for applications requiring wide band gaps, mechanical stability, and dielectric performance rather than photonic activity.

The antimony-based $(C_8H_{14}N_2)[SbCl_5]$, crystallizing in the monoclinic $P2_1/n$ space group, introduces additional complexity through its distinct metal center and coordination environment. The $Sb3^+$ ions adopt a nearly ideal square-pyramidal geometry within $[SbCl_5]^{2-}$ units, loosely aligned into pseudo-one-dimensional chains. The reduced coordination number (five *versus* six in Bi compounds) combined with the stereochemical activity of Sb's lone pair produces anisotropic bonding interactions, influencing both the electronic structure and dielectric response. This compound displays the lowest experimental band gap of the series (2.77 eV, theory 2.7 eV), consistent with its orbital contributions, and exhibits a prominent photoluminescence emission at 571 nm with broad spectral features extending from 250 to 800 nm, characteristic of mixed band-to-band and defect-assisted transitions. Dielectric spectroscopy further reveals complex relaxation phenomena with two thermally activated conductivity regimes (E_{a1} = 0.39 eV and E_{a2} = 0.97 eV), indicating dynamic dielectric behavior associated with coupled lattice and cationic motions. With a high packing efficiency of 92.9% (second only to Bi_2Br_{10}), $(C_8H_{14}N_2)[SbCl_5]$ exemplifies how subtle differences in coordination geometry and lone-pair activity can generate multifunctional properties combining low band gap, clear photoluminescence, and tunable dielectric response.

Across the series, several structure–property correlations emerge. The halide identity exerts a dominant influence on the electronic structure: Br^-, with its higher polarizability and larger radius, facilitates broader valence bands, narrower band gaps, and photoluminescent behavior, while Cl^- promotes electronic localization and transparency. The choice of metal cation is equally pivotal: substitution of Bi^{3+} by Sb^{3+} alters frontier orbital contributions and activates lone-pair-driven anisotropy, enhancing dielectric responses. Packing density and space group symmetry govern robustness and excitonic dynamics, with denser frameworks favoring stability but restricting radiative recombination. Although secondary to metal–halide connectivity, hydrogen bonding remains critical in modulating cohesion, dielectric relaxation, and fine-tuning optical gaps.

These correlations also extend to the biological domain, underscoring the multifunctional characteristic of hybrid halometallates. The same lattice parameters that tune optical band gaps and dielectric relaxation, such as halide polarizability, anion geometry, and packing density, directly govern antibacterial potency by modulating cation release and membrane accessibility. In this respect, **M41** uniquely combines a low band gap, visible-light photoluminescence, dynamic dielectric response, and superior antibacterial activity, positioning it as a genuine multifunctional platform. Such convergence of optoelectronic and biological functionality points to future applications beyond fundamental studies: Sb-based halometallates could be tailored as antimicrobial coatings for medical devices, integrated into photonic–biological hybrid systems, or deployed in responsive wound dressings where optical signaling and antibacterial action are simultaneously required. This multifunctional design philosophy highlights the potential of anion–cation engineering to generate hybrid materials that bridge solid-state chemistry with biomedical utility.

Altogether, the combined influence of metal–halide core geometry, halogen identity, and supramolecular architecture enables precise control over the optoelectronic and dielectric behavior of these hybrid halometallates. These findings establish a guiding framework for rational material design in future multifunctional applications. Furthermore, preliminary antibacterial

screenings suggest that packing density, electrostatic surface potential distribution, and hydrogen-bonding accessibility strongly mediate antimicrobial activity, with the superior performance of $(C_8H_{14}N_2)[SbCl_5]$ linked to its favorable lattice openness and efficient cation release.

4. Conclusion

This comparative investigation demonstrates that subtle variations in metal center, halide identity, and crystal packing exert a decisive influence on the multifunctional behavior of hybrid halometallates. The three investigated compounds, $(C_8H_{14}N_2)_2[Bi_2Br_{10}]\cdot 2H_2O$ (**M4**), $(C_8H_{14}N_2)_3[BiCl_6]_2$ (**M43**), and $(C_8H_{14}N_2)[SbCl_5]$ (**M41**), represent structurally distinct zero-dimensional frameworks that collectively illustrate how coordination geometry and supramolecular organization govern optical, dielectric, and biological properties within a unified organic environment.

Systematic structural and optical analyses reveal clear structure–property correlations across the series. The bromide-rich dimeric framework of **M4** favors broadband emission through enhanced lattice polarizability, whereas the highly distorted Bi–Cl environment in **M43** leads to a wider band gap and suppressed photoluminescence. In contrast, the Sb-based compound **M41** combines a relatively narrow band gap with well-defined emission and distinct dielectric relaxation behavior, highlighting the role of metal identity and coordination asymmetry in tuning electronic and dielectric responses. These observations are supported by complementary spectroscopic and theoretical analyses and emphasize the sensitivity of low-dimensional halometallates to targeted chemical substitution.

Beyond optoelectronic behavior, the antibacterial evaluation introduces an additional functional dimension. While the organic cation itself exhibits strong and broad-spectrum antibacterial activity, its incorporation into the hybrid lattice reveals that structural factors critically modulate biological performance. In particular, **M41** retains high antibacterial efficacy, whereas the more compact Bi-based frameworks significantly limit activity, underscoring the importance of lattice lability and ion-pair interactions. These interpretations are based on indirect structural and spectroscopic evidence, and further dedicated studies will be required to directly elucidate the active species and mechanisms involved. We note that a definitive deconvolution of pure halide *vs.* pure topology effects would require either the synthesis of an isostructural Bi–Cl dimer analogue or targeted TD-DFT/exciton calculations on a hypothetical Bi2Cl10 cluster. Because halide substitution often alters connectivity, these follow-up experiments are suggested for future study.

Overall, this work establishes a clear structure–property–function framework for Bi(III)- and Sb(III)-based hybrid halometallates and demonstrates that such materials can be rationally engineered to exhibit complementary optical, dielectric, and biological functionalities. The identification of **M41** as a multifunctional candidate provides proof of concept for the deliberate design of hybrid halometallates that extend beyond traditional optoelectronic roles, offering promising perspectives for future multifunctional and bio-integrated material systems.

Author contributions

Amin Alibi: conceptualization, data curation, formal analysis, methodology, visualization, writing – original draft, and writing – review & editing. Sameh Sellami and Fatma El Abed: investigation (antibacterial tests). Nour Elleuch: resources. Jerome Lhostec and Guillaume Duval: investigation (purity tests). Prof. Mohamed Boujelbene: resources, supervision, and validation.

Conflicts of interest

There are no conflicts to declare.

Data availability

Antibacterial inhibition zone diameters are the original experimental data of this work and are fully tabulated in the present manuscript. Supplementary information (SI) is available. See DOI: https://doi.org/10.1039/d5ma01261a.

CCDC 2384365 (**M4**), 2382366 (**M41**) and 2432091 (**M43**) contain the supplementary crystallographic data for this paper.[35a–c]

Acknowledgements

We sincerely thank Mrs Sameh DAMMAK, Principal Engineer of the Physics Department at the Faculty of Sciences, University of Sfax, for conducting the chemical analyses using FTIR and UV-visible spectroscopy.

References

1 D. B. Mitzi, Synthesis, Structure, and Properties of Organic–Inorganic Perovskites and Related Materials, *Prog. Inorg. Chem.*, 1999, **48**, 1–121, DOI: 10.1002/9780470166499.ch1.
2 B. E. Cohen, *et al.*, *Nat. Mater.*, 2020, **19**, 1036–1045.
3 Y.-X. Tan, F. Wang and J. Zhang, Design and synthesis of multifunctional metal–organic zeolites, *Chem. Soc. Rev.*, 2018, **47**, 3486–3510, DOI: 10.1039/C7CS00782E.
4 N. Wang, *et al.*, *Nat. Rev. Mater.*, 2020, **5**, 100–118.
5 Q. A. Akkerman, *et al.*, *Chem. Rev.*, 2019, **119**, 7189–7330.
6 G. Kieslich, S. Sun and A. K. Cheetham, An extended tolerance factor approach for organic–inorganic perovskites, *Chem. Sci.*, 2015, **6**, 3430–3433, DOI: 10.1039/C5SC00961H.
7 B. Saparov and D. B. Mitzi, Organic–Inorganic Perovskites: Structural Versatility for Functional Materials Design, *Chem. Rev.*, 2016, **116**, 4558–4596, DOI: 10.1021/acs.chemrev.5b00715.
8 J. Su, *et al.*, *ACS Energy Lett.*, 2021, **6**, 1249–1270.
9 W.-J. Yin, J.-H. Yang, J. Kang, Y. Yan and S.-H. Wei, Halide perovskite materials for solar cells: a theoretical review,

J. Mater. Chem. A, 2015, **3**, 8926–8942, DOI: 10.1039/C4TA05033A.

10 H. Wang and H. Wang, Advanced research on electrolytes for regulating the SEI in high-performance lithium metal batteries, *Adv. Funct. Mater.*, 2020, **30**, 1908701, DOI: 10.1039/D4EB00042K.

11 D. Ghosh, *et al.*, *Angew. Chem., Int. Ed.*, 2021, **60**, 19736–19756.

12 S. Wei, *et al.*, *Chem. Mater.*, 2020, **32**, 4782–4801.

13 M. D. Smith, B. A. Connor and H. I. Karunadasa, Tuning the Luminescence of Layered Halide Perovskites, *Chem. Rev.*, 2019, **119**, 3104–3139, DOI: 10.1021/acs.chemrev.8b00477.

14 W. Li, *et al.*, *Nano Energy*, 2018, **50**, 408–417.

15 M. Grätzel, The light and shade of perovskite solar cells, *Nat. Mater.*, 2014, **13**, 838–842, DOI: 10.1038/nmat4065.

16 N. Elleuch, S. Sellami, E. Toumi, C. Jridi, J. Lhoste, S. Shova and M. Boujelbene, New insights into bismuth(III)-based co-crystals with potential antibacterial activity: hydrothermal synthesis and comprehensive physico-chemical characterization, *J. Mol. Struct.*, 2026, **1351**, 144271, DOI: 10.1016/j.molstruc.2025.144271.

17 Z. Ouerghi, H. Gornitzka, E. Temel, I. Dridi and R. Kefi, A new non-centrosymmetric chlorobismuthate(III) hybrid material: crystal structure, optical properties and antibacterial study, *J. Mol. Struct.*, 2019, **1181**, 338–347, DOI: 10.1016/j.molstruc.2018.12.108.

18 E. Toumi, M. Siala, E. Khdhiri, N. Elleuch, S. Shova and M. Boujelbene, Comprehensive analysis of optical, vibrational and antibacterial properties of a novel antimony(III) halide semiconductor templated by 2-methylimidazole, *J. Mol. Struct.*, 2025, **1346**, 143104, DOI: 10.1016/j.molstruc.2025.143104.

19 A. Alibi, N. Elleuch, S. Shova, J. Lhoste, G. Duval and M. Boujelbene, Comprehensive structural and DFT analysis of a bismuth-based organic–inorganic hybrid material: vibrational, optical and photoluminescence properties of $(C_8H_{14}N_2)_2[Bi_2Br_{10}]\cdot 2H_2O$, *RSC Adv.*, 2025, **15**, 40439–40455, DOI: 10.1039/D5RA06614J.

20 A. Alibi, S. Shova, N. Elleuch and M. Boujelbene, *J. Mol. Struct.*, 2025, DOI: 10.1016/j.molstruct.2024.140857.

21 A. Alibi, N. Elleuch, S. Shova and M. Boujelbene, Comprehensive analysis of an antimony-based organic–inorganic hybrid material: structural, vibrational and Hirshfeld surface investigations of $(C_8H_{14}N_2)[SbCl_5]$, *J. Mol. Struct.*, 2025, **1324**, 140857, DOI: 10.1016/j.molstruc.2024.140857.

22 A. Alibi, N. Elleuch, A. Oueslati, S. Shova and M. Boujelbene, Synthesis, optical features, and electrical properties of a new antimony-based hybrid halide $(C_8H_{14}N_2)[SbCl_5]$, *RSC Adv.*, 2025, 54, DOI: 10.1039/D5RA06615H.

23 Rigaku Oxford Diffraction, CrysAlisPro Software System, version 1.171.38.46, Rigaku Corporation, 2017.

24 G. M. Sheldrick, Crystal structure refinement, *Acta Crystallogr. C*, 2015, **71**, 3–8, DOI: 10.1107/S2053229614024218.

25 G. M. Sheldrick, Crystal structure determination, *Acta Crystallogr. A*, 2015, **71**, 3–8, DOI: 10.1107/S2053273314026370.

26 M. J. Frisch*et al.*, *Gaussian 09, Revision D.01*, Gaussian, Inc., Wallingford CT, 2016.

27 N. Zhanpelsov, M. Matsuoka, H. Yamashita and M. Anpo, *J. Phys. Chem. B*, 1998, **102**, 6915–6922.

28 N. Niclasc, M. Dolg, H. Stoll and H. Preuss, *J. Chem. Phys.*, 1995, **102**, 8942–8952.

29 T. Lu and F. Chen, Multiwfn: A multifunctional wavefunction analyzer, *J. Mol. Struct.*, 2012, **1006**, 84–92, DOI: 10.1002/jcc.22885.

30 R. Dennington, T. A. Keith and J. M. Millam, *GaussView*, Semichem Inc., Shawnee Mission KS, 2016.

31 M. Hafez, I. S. Yahia and S. Taha, Diffuse reflectance and structural analysis of $ZnO–SiO_2$ nanocomposites, *Spectrochim. Acta A*, 2014, **127**, 521–528, DOI: 10.1016/j.saa.2014.02.094.

32 K. SowriBabun, A. R. Reddy, C. Sujatha and K. V. Reddy, *Ceram. Int.*, 2013, **39**, 3055–3063.

33 Z. Ouerghi, H. Gornitzka, E. Temel, I. Dridi and R. Kefi, A new non-centrosymmetric chlorobismuthate(III) hybrid material: crystal structure, optical properties and antibacterial study, *J. Mol. Struct.*, 2019, **1181**, 338–347, DOI: 10.1016/j.molstruc.2018.12.108.

34 S. Ben Ali, A. Feki, V. Ferretti, M. Nasri and M. Belhouchet, Crystal structure, spectroscopic, optical, thermal and biological properties of a bismuth(III) iodide hybrid material, *RSC Adv.*, 2020, **10**, 35174–35184, DOI: 10.1039/D0RA05646D.

35 (*a*) CCDC 2384365: Experimental Crystal Structure Determination, 2025, DOI: 10.5517/ccdc.csd.cc2l140t; (*b*) CCDC 2382366: Experimental Crystal Structure Determination, 2025, DOI: 10.5517/ccdc.csd.cc2kz1j4; (*c*) CCDC 2432091: Experimental Crystal Structure Determination, 2025, DOI: 10.5517/ccdc.csd.cc2mmskm.